

Exoplanet Detection Methods

Jason T. Wright, B. Scott Gaudi

October 11, 2012

Abstract

This chapter reviews various methods of detecting planetary companions to stars from an observational perspective, focusing on radial velocities, astrometry, direct imaging, transits, and gravitational microlensing. For each method, this chapter first derives or summarizes the basic observable phenomena that are used to infer the existence of planetary companions, as well as the physical properties of the planets and host stars that can be derived from the measurement of these signals. This chapter then outlines the general experimental requirements to robustly detect the signals using each method, by comparing their magnitude to the typical sources of measurement uncertainty. This chapter goes on to compare the various methods to each other by outlining the regions of planet and host star parameter space where each method is most sensitive, stressing the complementarity of the ensemble of the methods at our disposal. Finally, there is a brief review of the history of the young exoplanet field, from the first detections to current state-of-the-art surveys for rocky worlds.

Contents

1	Basic Principles of Planet Detection	2
1.1	Spectroscopic Binaries and Orbital Elements	3
1.2	Radial Velocities	6
1.3	Astrometry	8
1.4	Imaging	9
1.5	Transits	11
1.6	Gravitational Microlensing	13
1.7	Timing	16
2	The Magnitude of the Problem	17
2.1	Radial Velocities	18
2.2	Astrometry	19
2.3	Imaging	20
2.4	Transits	23
2.5	Microlensing	25
2.6	Timing	27

3	Comparisons of the Methods	27
3.1	Sensitivities of the Methods	28
3.2	Habitable Planets	33
4	Early Milestones in the Detection of Exoplanets	37
4.1	Van de Kamp and Barnard's Star	37
4.2	PSR 1257+12 and the Pulsar Planets	37
4.3	Early Radial Velocity Work	38
4.3.1	Campbell & Walker's survey and γ Cep Ab	38
4.3.2	Latham's survey and HD 114762 <i>b</i>	39
4.3.3	Marcy & Butler's iodine survey	41
4.3.4	Hatzes & Cochran's survey and β Gem <i>b</i>	43
4.3.5	Mayor & Queloz and 51 Pegasi <i>b</i>	43
4.4	The First Planetary Transit: HD 209458 <i>b</i>	44
4.5	Microlensing	44
4.5.1	Microlensing History	44
4.5.2	First Planet Detections with Microlensing	45
5	State of the Art	46
5.1	Astrometry	46
5.2	Imaging	48
5.2.1	2M1207 <i>b</i>	48
5.2.2	Fomalhaut <i>b</i>	48
5.2.3	Beta Pictoris <i>b</i>	50
5.2.4	The HR 8799 Planetary System	50
5.2.5	SPHERE, GPI, and Project 1640	51
5.3	Rocky and Habitable Worlds	51
5.3.1	HARPS, Keck/HIRES, and the Planet Finding Spectrograph	51
5.3.2	Space-Based Transit Surveys	52
5.3.3	Second Generation Microlensing Surveys	54
6	Conclusions	54

1 Basic Principles of Planet Detection

This chapter begins by reviewing the basic phenomena that are used to detect planetary companions to stars using various methods, namely radial velocities, astrometry, transits, timing, and gravitational microlensing. It derives the generic observables for each method from the physical parameters of the planet/star system. These then determine the physical parameters that can be inferred from the planet/star system for the general case.

Notation with subscripts $*$ and p refer to quantities for the star and planet, respectively. Therefore, a star has mass M_* , radius R_* , mean density ρ_* , surface gravity g_* , and effective temperature T_* , and is orbited by a planet of mass M_p , radius R_p , density ρ_p , temperature T_p , and surface gravity g_p . The orbit has a semimajor axis a , period P , and eccentricity e .

1.1 Spectroscopic Binaries and Orbital Elements

Exoplanet detection is essentially the extreme limit of binary star characterization, and so it is unsurprising that the terminology and formalism of planetary orbits derives from that of binaries.

Conservation of momentum requires that as a planet orbits a distant star, the star executes a smaller, opposite orbit about their common center of mass. The size (and velocity) of this orbit is smaller than that of the planet by a factor of the ratio of their masses. The component of this motion along the line of sight to the Earth can, in principle, be detected as a variable radial velocity. The mass of the exoplanet can be calculated from the magnitude of the radial velocity (RV) or astrometric variations and from the mass of the star, determined from stellar models and spectroscopy or astrometry.

Two mutually orbiting bodies revolve in ellipses about a common center of mass, the origin of our coordinate system. Orbital angles in the plane of the bodies' mutual orbit are measured with respect to the line of nodes, formed by the intersection of the orbital plane with the plane of the sky (i.e. the plane perpendicular to a line connecting the observer to the system's center of mass). The position of this line on the sky has angle Ω , representing the position angle (measured east of north) of the ascending (receding) node, where the star (and planet) cross the plane of the sky moving away from Earth. Figure 1 illustrates the other orbital elements in the problem. As indicated, the orientation of the each orbital ellipse with respect to the plane of the sky is specified by the longitude of periastron, ω , which is the angle between the periastron¹ and the ascending node along the orbit in the direction of the motion of the body. Since the orbit of the star is a reflection about the origin of the orbit of the exoplanet, the orbital parameters of the planet are identical to that of the star except that the longitudes of periastron differ by π : $\omega_p = \omega_* + \pi$.

The physical size of the ellipse, given by the semi-major axis, a , is set by Newton's modification of Kepler's third law of planetary motion:

$$P^2 = \frac{4\pi^2}{G(M_* + M_p)} a^3 \quad (1)$$

The semimajor axis is $a = a_* + a_p$, where a_* and a_p are the semi-major axes of the two bodies' orbits with respect to the center of mass, given by,

$$a_* = \frac{M_p}{M_* + M_p} a; \quad a_p = \frac{M_*}{M_* + M_p} a \quad (2)$$

The position of either body in its orbit about the origin can be expressed in polar coordinates (r, ν) , where ν is the true anomaly, the angle between the location of the object and the periastron. The separation between the star and planet is given by

$$r(1 + e \cos \nu) = a(1 - e^2) \quad (3)$$

where e is called the eccentricity of the orbit, and has the domain $[0, 1)$ for bound orbits. The observed eccentricities of exoplanets are quite varied: eccentricities above 0.9 have been seen in a few cases, and eccentricities above 0.3 are common, at least for Jovian exoplanets Wright et al. (2011). Figure 2 illustrates the physical shape of such orbits.

¹Periastron marks the point where the two bodies have their closest approach.

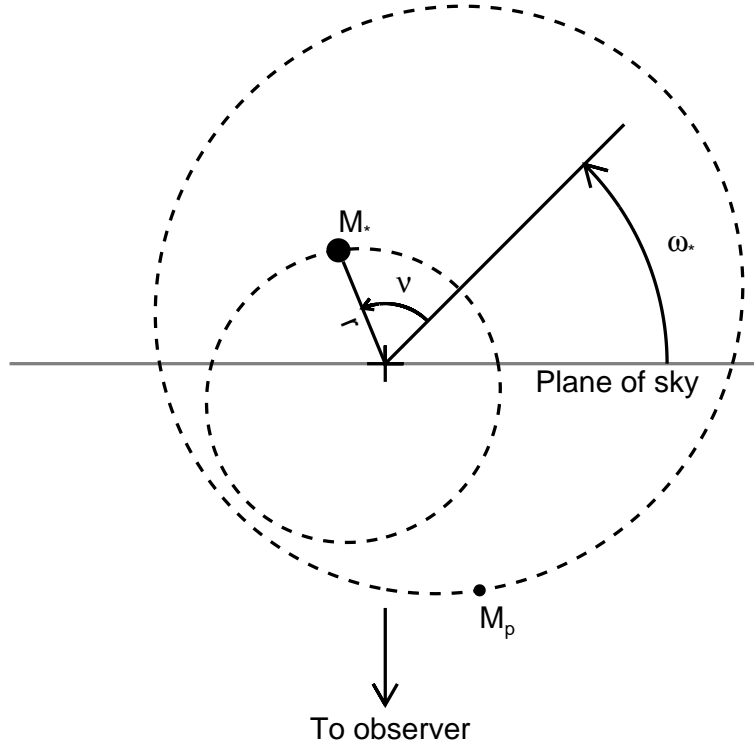


Figure 1: Elements describing orbital motion in a binary with respect to the center of mass (cross). The argument of periastron ω is measured from the ascending (receding) node, and the true anomaly ν is measured with respect to the periastron. Both angles increase along the direction of the star's motion in the plane of the orbit. The longitude of the periastron of the star ω_* is indicated. At a given time in the orbit, the true anomalies of the planet and star are equal, where as the longitude of periastron of the planet is related to that of the star by $\omega_p = \omega_* + \pi$. In Doppler planet detection, the orbital elements of the star are conventionally reported, from which the orbital elements of the planet can be inferred.

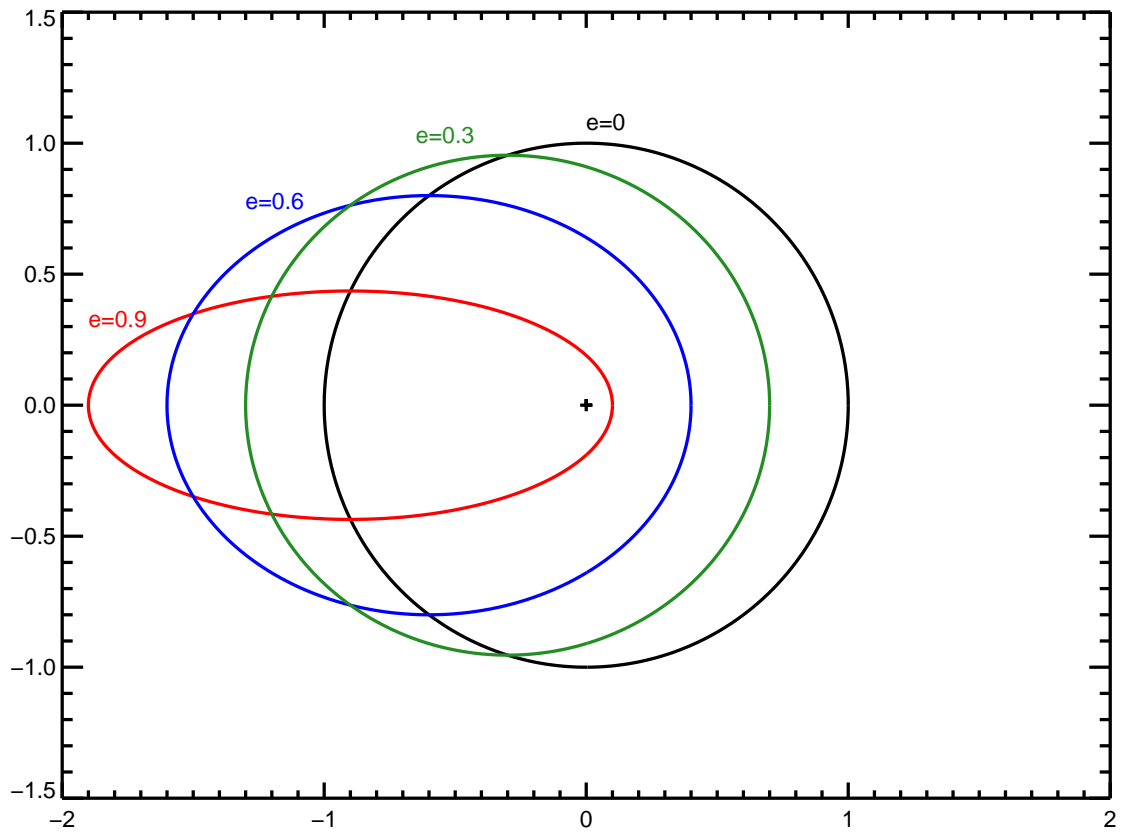


Figure 2: Shape of various eccentric orbits in the orbital plane. A handful of exoplanets with eccentricities above 0.9 have been detected.

Practical computation of a body's position in its orbit with time is usually performed through the intermediate variable E , called the eccentric anomaly. E is related to the time since periastron passage T_0 through the mean anomaly, M :

$$M = \frac{2\pi(t - T_0)}{P} = E - e \sin E \quad (4)$$

and allows the computation of ν through the relation

$$\tan \frac{\nu}{2} = \sqrt{\frac{1+e}{1-e}} \tan \frac{E}{2} \quad (5)$$

The eccentric anomaly is also useful because it is simply related to r :

$$E = \arccos \frac{1 - r/a}{e} \quad (6)$$

1.2 Radial Velocities

The radial reflex motion of a star in response to an orbiting planet can be measured through precise Doppler measurement, and this motion reveals the period, distance and shape of the orbit, and provides information about the orbiting planet's mass. (The treatment of RV and astrometric measurement below follows Wright & Howard (2009)).

Six parameters determine the functional form of the periodic radial velocity variations and thus the observables in a spectroscopic orbit of the star: P , K , e , ω_* , T_0 , and γ (it is convention in the Doppler-detection literature to refer to ω without its $*$ subscript, but it is standard to report the star's argument of periastron, not the planet's).

$$V_r = K[\cos(\nu + \omega_*) + e \cos \omega_*] + \gamma \quad (7)$$

with ν related to P , e , and T_0 through E . The semi-amplitude of the signal in units of velocity is K (the peak-to-trough RV variation is $2K$). The bulk velocity of the center of mass of the system is given by γ .

For circular orbits $e = 0$, there is no periastron approach, and so T_0 and ω_* are formally undefined; in such cases a nominal value of ω_* (such as 0 or $\pi/2$) sets T_0 (alternatively, one can specify the value of one of the angles at a given epoch).

In short, the variables P , T_0 , and K respectively set the period, phase, and amplitude of an RV curve, while the variables ω_* and e determine the shape of the radial velocity signature of an orbiting companion, as shown in Figure 3. Characterization of the orbits of single unseen companions, such as exoplanets, is ultimately an exercise in fitting observed radial velocities to the family of curves in Figure 3 to determine the six orbital parameters.

Two additional orbital parameters complete the description of a planet's orbit: the inclination of the orbit, i , which determines the angle between the orbital plane and the plane of the sky, such that $i = 0$ corresponds to a face-on, counter-clockwise orbit, and Ω , the longitude of the ascending node. These parameters cannot be determined with radial velocity observations alone, and can only be measured through astrometry, where the angular displacement of the star on the sky is directly measured.

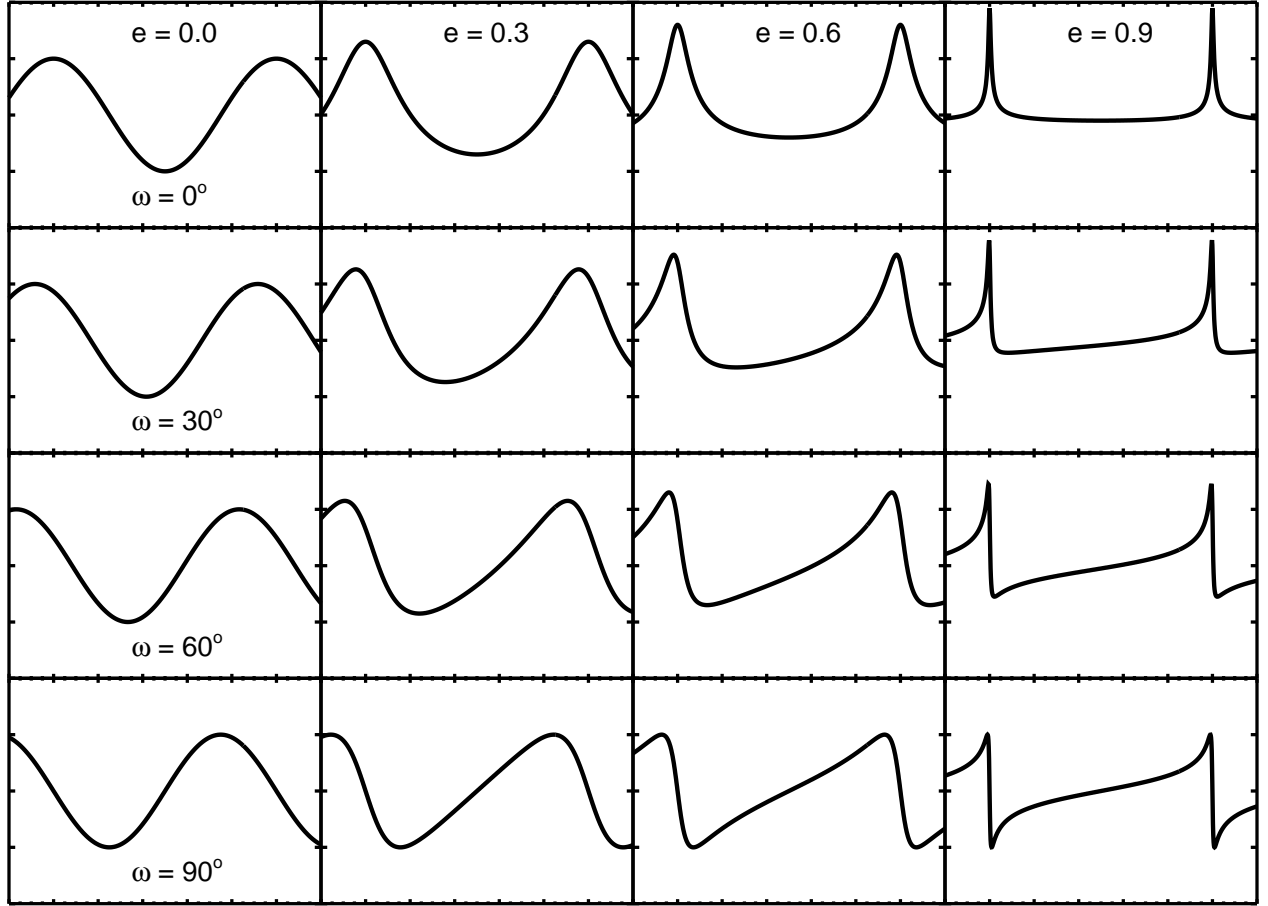


Figure 3: The effects of e and ω_* on radial velocity curves. These curves have been scaled to unit K and common P and T_0 . Each column shows curves of constant e and each row curves of constant ω_* as indicated. Other quadrants of ω_* yield reflections of these curves.

The effect of the inclination of the orbit is to reduce the radial component of the velocity of the star by $\sin i$. The fundamental observable of a spectroscopic binary which constrains the physical properties of system is thus

$$\frac{PK^3(1-e^2)^{\frac{3}{2}}}{2\pi G} = \frac{M_p^3 \sin^3 i}{(M_p + M_*)^2} \quad (8)$$

where G is Newton's gravitational constant. The right hand side of this equation is known as the *mass function* of the system. For exoplanets where M_* can be estimated from stellar models, the minimum value for M_p (i.e. its value for $\sin i = 1$, or an edge-on orbit) is called the “minimum mass” of the planet, and is usually labeled “ $M_p \sin i$ ” for succinctness (since when $M_p \ll M_*$ its small correction to the denominator is negligible, though not ignored). The true mass of the detected exoplanet is thus higher by a factor of $1/\sin i$, which has a typical (median) value of 1.15 for randomly oriented orbits (all other things being equal).

1.3 Astrometry

Plane-of-sky variations in a star's position provide both redundant and complementary information to radial velocities, yielding the true inclination and orientation of a planetary orbit. Astrometry of the orbits of well-separated binary stars of similar magnitude is a matter of careful instrument calibration to precisely measure the separation and position angle between the stars. For exoplanet detection, the problem is to detect the motions around a star about an unseen companion with respect to a set of (presumably) stable background stars.

For an orbit with semimajor axis a_* of a star at distance d from the Earth, producing an astrometric signal of semi-amplitude $\theta_* = a_*/d$, astrometric orbits can be described in terms of the Thiele-Innes constants

$$A = \theta_* (\cos \Omega \cos \omega_* - \sin \Omega \sin \omega_* \cos i) \quad (9)$$

$$B = \theta_* (\sin \Omega \cos \omega_* + \cos \Omega \sin \omega_* \cos i) \quad (10)$$

$$F = \theta_* (-\cos \Omega \sin \omega_* - \sin \Omega \cos \omega_* \cos i) \quad (11)$$

$$G = \theta_* (-\sin \Omega \sin \omega_* + \cos \Omega \cos \omega_* \cos i) \quad (12)$$

$$C = \theta_* \sin \omega_* \sin i \quad (13)$$

$$H = \theta_* \cos \omega_* \sin i \quad (14)$$

which can be quickly computed using rotation matrices:

$$\begin{bmatrix} A & B & C \\ F & G & H \\ \theta_* \sin i \sin \Omega & -\theta_* \sin i \cos \Omega & \theta_* \cos i \end{bmatrix} = \theta_* R_z(\omega_*) R_x(i) R_z(\Omega) \quad (15)$$

where R is the 3-D rotation matrix, given in the case of the z -axis by

$$R_z(\Omega) = \begin{bmatrix} \cos \Omega & \sin \Omega & 0 \\ -\sin \Omega & \cos \Omega & 0 \\ 0 & 0 & 1 \end{bmatrix} \quad (16)$$

The Thiele-Innes constants are related back to Keplerian orbital elements with the relations:

$$\tan(\omega_* + \Omega) = \frac{B - F}{A + G} \quad (17)$$

$$\tan(\omega_* - \Omega) = \frac{-(B + F)}{A - G} \quad (18)$$

$$\tan^2\left(\frac{i}{2}\right) = \frac{(A - G) \cos(\omega_* + \Omega)}{(A + G) \cos(\omega_* - \Omega)} \quad (19)$$

$$\theta_* = \frac{(A \cos \omega_* - F \sin \omega_*) \cos \Omega - (A \sin \omega_* + F \cos \omega_*) \sin \Omega \sec i}{\quad} \quad (20)$$

$$\theta_*^2 = A^2 + B^2 + C^2 = F^2 + G^2 + H^2 \quad (21)$$

The quantities ω_* and Ω have a $\pm\pi$ ambiguity that is resolved with radial velocity measurements, without which convention dictates that we choose $\Omega < \pi$.

The C and H constants are related the radial component of the motion. These constants can be combined with the elliptical rectangular coordinates, defined as

$$X = \cos E - e \quad (22)$$

$$Y = \sqrt{1 - e^2} \sin E \quad (23)$$

to describe the astrometric displacements of a star in the North ($\Delta\delta$) and East ($\Delta\alpha \cos \delta$) directions:

$$\begin{aligned} \Delta\delta &= AX + FY \\ \Delta\alpha \cos \delta &= BX + GY \end{aligned} \quad (24)$$

and the magnitude of the astrometric offset from the apparent center of mass is (for small offsets) $\Delta\theta_* \equiv [\Delta\delta^2 + (\Delta\alpha \cos \delta)^2]^{1/2}$. In practice, astrometric motions are small perturbations on the much larger parallactic and proper motions.

1.4 Imaging

The direct detection of planets is the most conceptually straightforward method of detection: essentially one seeks simply to directly detect photons from the exoplanet, resolved from those of the parent star. Although the emission of exoplanets is indeed quite faint, it is generally the problem of detecting this emission in the proximity of the much brighter stellar source that presents the most severe practical obstacle to direct detection. The disentangling of stellar and planetary photons is an imperfect process that is easiest at wider separations. The efficiency of this disentangling ultimately determines the detection thresholds of an instrument. Therefore, the most important parameters of the exoplanet for determining the difficulty of direct detection are the planet/star flux ratio f_p and the angular separation between the planet and star. Typically, contrast limits worsen at smaller angular separations.

The angular separation of the planet and star on the sky is given by

$$\Delta\theta = r_\perp / d \quad (25)$$

where r_\perp is the projected separation of the planet from the star, and d is the distance to the system. By definition, if d is in parsecs and r_\perp in AU, then θ is in arcseconds. In general,

$\Delta\theta = (1 + M_*/M_p)\Delta\theta_* = (1 + M_*/M_p)\sqrt{(BX + GY)^2 + (AX + FY)^2}$. For circular orbits, this reduces to $r_\perp = a(\cos^2\beta + \sin^2\beta \cos^2 i)^{1/2}$, where $\beta = \nu + \omega_p$ is the angle between the position of the planet along its orbit relative to the ascending node. Planets typically orbit stars at distances from hundredths to hundreds of AU. For a hypothetical giant planet orbiting 5 AU from a nearby star sitting at 50 pc, this corresponds to a maximal angular separation of 100 mas.

The emission from an exoplanet can generally be separated into two sources: stellar emission reflected by the planet surface and/or atmosphere, and thermal emission from the planet. Thermal emission can be due to either “intrinsic” thermal emission (e.g. the fossil heat of formation), or thermal emission from reprocessed stellar luminosity. Exoplanets may also produce some non-thermal emission, which we will not consider here.

The reflected light will have a spectrum that is broadly similar to that of the star, with additional features arising from the planetary surface and/or atmosphere. Therefore, for solar-type stars, this reflected emission generally peaks at optical wavelengths. The monochromatic planet/star flux ratio for reflected light can generally be written (e.g., Seager 2010),

$$f_{\text{ref},\lambda} = A_{g,\lambda} \left(\frac{R_p}{a} \right)^2 \Phi_{\text{ref},\lambda}(\alpha) \quad (26)$$

where $A_{g,\lambda}$ is the monochromatic geometric albedo, and $\Phi_{\text{ref},\lambda}$ is the reflected light phase curve, which depends on the planetary phase angle α (the star-planet-observer angle) and the wavelength λ . The geometric albedo is defined as the ratio of the flux emitted from the planet at $\alpha = 0$ relative to that of a perfectly and isotropically scattering uniform disk of equal solid angle. For a circular orbit, $\cos\alpha = \sin\beta \sin i$.

Assuming that the thermal emission from the planet has a roughly blackbody spectrum, the flux ratio is

$$f_{\text{therm},\lambda} = \left(\frac{R_p}{R_*} \right)^2 \frac{B_\lambda(T_p)}{B_\lambda(T_*)} \Phi_{\text{therm},\lambda}(\alpha) \rightarrow \left(\frac{R_p}{R_*} \right)^2 \frac{T_p}{T_*} \Phi_{\text{therm},\lambda}(\alpha), \quad (27)$$

where $\Phi_{\text{therm},\lambda}$ is the monochromatic thermal phase curve. For observations in the Rayleigh-Jeans tail of the blackbody, $\lambda \gg hc/(k_b T)$, and thus $B_\lambda(T) \propto T$, yielding the limit shown in Equation 27. If the planet is in thermal equilibrium with the stellar radiation, then $T_p = T_{\text{eq}}$ and

$$\frac{T_{\text{eq}}}{T_*} = \left(\frac{R_*}{a} \right)^{1/2} [f(1 - A_B)]^{1/4}, \quad (28)$$

where A_B is the Bond albedo, the fraction of the total energy incident on the planet that is not absorbed, and f accounts the fraction of the entire planet surface over which the absorbed energy is re-emitted, i.e. $f = 1/4$ if the thermal energy is emitted over the entire 4π of the planet. Of course, planets may be self-luminous as well, particularly if they are young and have retained significant residual heat from formation.

The form for $\Phi_{\text{ref},\lambda}$ depends on the scattering properties of the planetary atmosphere. For the case of a Lambert sphere that scatters all incident radiation equally in all directions,

$$\Phi_{\text{Lambert},\lambda} = \frac{1}{\pi} [\sin\alpha + (\pi - \alpha) \cos\alpha]. \quad (29)$$

Also for a Lambert sphere, $A_B = 1$ and $A_g = 2/3$. The form for $\Phi_{\text{therm},\lambda}$ depends on the surface brightness distribution of the planet, which in turn depends on the amount of heat

redistribution. For the case of a tidally-locked planet in which the absorbed radiation is promptly and locally re-emitted, the phase curve has the same form as for a Lambert sphere (Seager 2010).

Resolved emission of an planet/star system is essentially equivalent to a visual binary. Once the overall scale of the system has been set, measurements of the position of the planet relative to the star at a sufficient number of epochs yield all of the orbital elements of the system, up to the 2-fold degeneracy in orientation with respect to the sky discussed previously. The scale of the system can be set either by an estimate of the distance to the system, or by an external estimate of the primary mass M_* (under the assumption $M_p \ll M_*$). For reflected light measurements, only the product of the geometric albedo and planet cross section can be determined; estimating the planet radius independently generally requires an assumption about the albedo. For thermal light measurements, the temperature T_p can (in principle) be estimated from the flux at multiple wavelengths, and then the surface brightness can be estimated from T_p , and thus the radius can be inferred from the planetary flux. The planet mass cannot be determined from the planet flux or its relative orbit, and must be inferred indirectly through coupled atmosphere/evolutionary models. In some favorable cases, mutual gravitational perturbations in multiplanet systems may allow the determination of the planet masses directly.

Of course, the real power of direct imaging lies in the ability to acquire spectra of the planets once they are discovered, and thus characterize the constituents of the planetary atmosphere. This provides one of the only feasible routes to assessing the habitability of terrestrial planets in the Habitable Zones (Kasting et al. 1993) of the parent stars, and likely the *only* feasible route to do so for Earthlike planets orbiting solar-type stars.

1.5 Transits

The presence of a planetary companion to a star gives rise to a multitude of physical phenomena that manifest themselves via temporal variations of the flux of the system relative to that of an otherwise identical isolated star. Typically the largest of these occurs if a fortunate alignment allows a planet to transit (pass in front of) its host star from our perspective. In this case, the star will exhibit brief, periodic dimmings which signal the presence of the planet. Transits offer a intriguingly simple way to detect planets.

The condition for a transit is roughly that the projected separation between the planet and host star at the time of inferior conjunction of the planet is less than the sum of the radii of planet and star, i.e., $r(t_c) \cos i \leq R_* + R_p$, where $r(t_c)$ is the separation of the planet from the host star at conjunction, and R_* and R_p are the radii of the star and planet, respectively. Given the definition of ω_* , $r(t_c) = a(1 - e^2)/(1 + e \sin \omega_*)$, and so transits occur when the impact parameter of the planet's orbit with respect to the star in units of the host radius,

$$b \equiv \frac{a \cos i}{R} \frac{1 - e^2}{1 + e \sin \omega_*}, \quad (30)$$

is less than the sum of the (normalized) radii, $b \leq 1 + k$, where $k \equiv R_p/R_*$. Integrating over i assuming isotropic orbits and thus a uniform distribution of $\cos i$ yields the *transit probability*,

$$P_{\text{tr}} \equiv \left(\frac{R_* + R_p}{a} \right) \frac{1 + e \sin \omega_*}{1 - e^2}. \quad (31)$$

For a circular orbit and assuming $k \ll 1$, this reduces to the simple expression $P_{\text{tr}} = R_*/a$. Note that in these expressions, we have used the longitude of the periastron of the orbit of star rather than the (perhaps more intuitive) value for the planet, because the former is generally adopted for fits to the stellar reflex radial velocity data.

When the planet transits in front of its parent star, the flux of the star will decrease by an amount that is proportional to the ratio of the areas of the planet and star. For the purposes of exposition, in the following we will assume a circular orbit, uniform host surface brightness, and $R_p \ll R_* \ll a$ and $M_p \ll M_*$. In the general case of a limb-darkened star, eccentric orbit, and arbitrary scales for R_p , R_* and a , the expressions for the shape of the transit are considerably more complicated, as are the arguments for the kinds of information that can be extracted from transit and RV signals (see Winn 2010 and references therein). However, the basic structure of the problem is the same under our approximations, and what follows serves to illustrate the essential concepts.

Under these assumptions, the planet follows a rectilinear trajectory across the face of the star with an impact parameter b , and the transit signature will have an approximately trapezoidal shape, which can be characterized by the duration T , ingress/egress time τ , and fractional flux depth δ . The depth of the transit relative to the out-of-transit flux is

$$\delta = k^2. \quad (32)$$

The duration of the transit can be quantified by its full-width at half-maximum, which is roughly the time interval T between the two points where the center of the planet appears to touch the edges of the star. This is approximately,

$$T \simeq T_{\text{eq}}(1 - b^2)^{1/2}, \quad (33)$$

where it is useful to define the equatorial crossing time (i.e., the transit duration for $b = 0$),

$$T_{\text{eq}} \equiv \frac{R_* P}{\pi a} = f_{\text{tr}} P \simeq \left(\frac{3P}{\pi^2 G \rho_*} \right)^{1/3}. \quad (34)$$

Here ρ_* is the mean density of the host star, and $f_{\text{tr}} \equiv P/\pi a = P_{\text{tr}}/\pi$ is the transit *duty cycle*, or the fraction of planet orbit in transit. The last equality, which assumes $M_p \ll M_*$, also implies that, to an order of magnitude, the equatorial transit duration is the cube root of the product of the orbital period and the stellar dynamical or free-fall time ($t_{\text{dyn}} \sim (G\rho_*)^{-1/2}$) squared.

The ingress/egress time (these are equal for a circular orbit) τ is the time between when the edge of the planet just appears to touch the star for the first and second time (ingress, or the time between first and second “contact”) or third and fourth time (egress, the time between third and fourth “contact”), and is given by,

$$\tau \sim T_{\text{eq}} \delta^{1/2} (1 - b^2)^{-1/2}. \quad (35)$$

One of the most useful aspects of transiting planets is that, when combined with radial velocity data, they allow one to infer the masses and radii of the star and planet up to a one-parameter degeneracy, as follows. Measuring T , t , and δ from a single transit allows one to infer b , T_{eq} , and k

$$b^2 = 1 - \delta^{1/2} \frac{T}{\tau}, \quad T_{\text{eq}}^2 = \frac{T\tau}{\delta^{1/2}}, \quad k = \delta^{1/2}, \quad (36)$$

The impact parameter is related to the orbital inclination i via $b = a \cos i / R_*$, but a and R_* cannot be determined from light curves alone. With the detection of multiple transits, one can further infer the period P , and thus the stellar density ρ_* via Equation 34. As reviewed in §1.2, the reflex radial velocity orbit of the star allows one to infer K and P which can be combined to determine the mass function, $\sim (M_* \sin i)^3 / M_*^{2/3}$, but a determination of the planet mass requires both a measurement of i and M_* . Thus one additional parameter is needed to break the degeneracy and set the overall scale of the system. This can be accomplished by imposing external constraints on the properties of the primary, either through parameters measured from high-resolution spectroscopy or parallax, or invoking theoretical relations between the mass and radius of the star through isochrones, or both. For illustration, if we assume the primary mass is precisely known, then we can infer R_* through ρ_* , and a through P , and thus determine i from the impact parameter measurement. Finally, we can measure R_p from k , and the planet mass from the mass function, i , and M_* .

1.6 Gravitational Microlensing

The gravitational microlensing method detects planets via the direct gravitational perturbation of a background source of light by a foreground planet. When a foreground compact object (either a star or stellar remnant) happens to pass very close to our line-of-sight to a more distant star, the light from the background star will be split into two images. These images are typically unresolved, but they are magnified by an amount that depends on the angular separation between the lens and source. Since this separation is a function of time, the background source exhibits a smooth, symmetric time-variable magnification: a microlensing event. If the foreground lens happens to have a planetary companion and the planetary companion happens to have a projected separation from the primary lens near the paths of the two primary images, the gravity of the planet will further perturb the light, resulting in a short-lived perturbation from the primary microlensing event, revealing the planetary companion. Free floating planets and planets widely separated from their parent star can also be detected as isolated, short timescale microlensing events.

Consider a planet/star system acting as a lens located at a distance d and source located at a distance d_s . Light from the source is deflected, split into multiple images, and magnified by the gravity of the foreground lens. The fundamental equation that is used to derive the observable properties of a gravitational microlensing event is the *lens equation*, which relates the angular separation β between the lens and source in the absence of lensing to the angular positions θ of the images of the source created due to lensing. For a general lens system, these are vector quantities, but for a single lens the lens, source, and image positions are all co-linear, so we can drop the vector notation. The lens equation for an isolated point lens is (Einstein 1936),

$$\beta = \theta - \frac{4GM_*}{c^2 d_{\text{rel}} \theta}, \quad (37)$$

where $d_{\text{rel}}^{-1} \equiv d^{-1} - d_s^{-1}$. If the lens and source are perfectly aligned ($\beta = 0$), the source is imaged into a ring of radius equal to,

$$\theta_E \equiv \left(\frac{4GM_*}{d_{\text{rel}} c^2} \right)^{1/2} \simeq 713 \mu\text{as} \left(\frac{M}{0.5 M_\odot} \right)^{1/2} \left(\frac{d_{\text{rel}}}{8 \text{ kpc}} \right)^{-1/2}. \quad (38)$$

The Einstein ring radius is the fundamental scale of gravitational microlensing, and depends on the distances to the lens and source, and the mass of the lens. At the distance of the lens, the linear Einstein ring radius is

$$r_E \equiv \theta_E d \simeq 2.85 \text{AU} \left(\frac{M_*}{0.5 M_\odot} \right)^{1/2} \left(\frac{d_s}{8 \text{kpc}} \right)^{1/2} \left[\frac{x(1-x)}{0.25} \right]^{1/2}, \quad (39)$$

where $x \equiv d/d_s$.

Normalizing by θ_E , the lens Equation 37 simplifies to,

$$u = y - y^{-1}, \quad (40)$$

where $u \equiv \beta/\theta_E$ and $y \equiv \theta/\theta_E$. If $u \neq 1$, this has two solutions, $y_{\pm} = \pm \frac{1}{2}(\sqrt{u^2 + 4} \pm u)$, and thus in general an isolated point lens creates two images. One of these images is always separated by more than θ_E from the lens ($y_+ \geq 1$), and the other is always separated by less than θ_E ($|y_-| \leq 1$). The separation between the two images is $\sim 2\theta_E$ and thus they are typically unresolved. Because the images are distorted relative to the source, they are also (de-)magnified. The total magnification for the sum of the two unresolved images is,

$$A(u) = \frac{u^2 + 2}{u\sqrt{u^2 + 4}}. \quad (41)$$

The magnification increases for decreasing u (better source-lens alignment), and formally diverges as $u \rightarrow 0$ for a point source.

The source, lens, and observer are all in relative motion, and thus the angular separation between the source and lens is a function of time: a microlensing event. If we approximate the relative proper motion μ_{rel} of the lens and source as constant, then we can parametrize the trajectory of the source relative to the lens as,

$$u(t) = \left[\left(\frac{t - t_0}{t_E} \right)^2 + u_0^2 \right]^{1/2}, \quad (42)$$

where u_0 is the dimensionless angular separation at the time of closest approach to the lens (the impact parameter), t_0 is the time when $u = u_0$ (also the time of maximum magnification for a point lens), and t_E is the Einstein ring crossing time,

$$t_E \equiv \frac{\theta_E}{\mu_{\text{rel}}}. \quad (43)$$

Figure 4 shows the source positions, image positions, and magnification of an example single lens microlensing event with $u_0 = 0.2$. In general, the magnification as a function of time for a single lens event has a smooth, symmetric form that is described by three parameters (t_E, t_0, u_0) . Events with lower u_0 lead to more distorted images and higher magnification near peak. For $u_0 \ll 1$, the peak magnification is $A_{\text{max}} \propto u_0^{-1}$. Events with $A_{\text{max}} \gtrsim 100$ are typically referred to as “high magnification events.”

Planetary companions to the lens star can be detected in a microlensing event if they happen to have a projected separation in the paths of one or both of the images created by the primary lens. As the image sweeps by the planet, the gravity of the planet will further

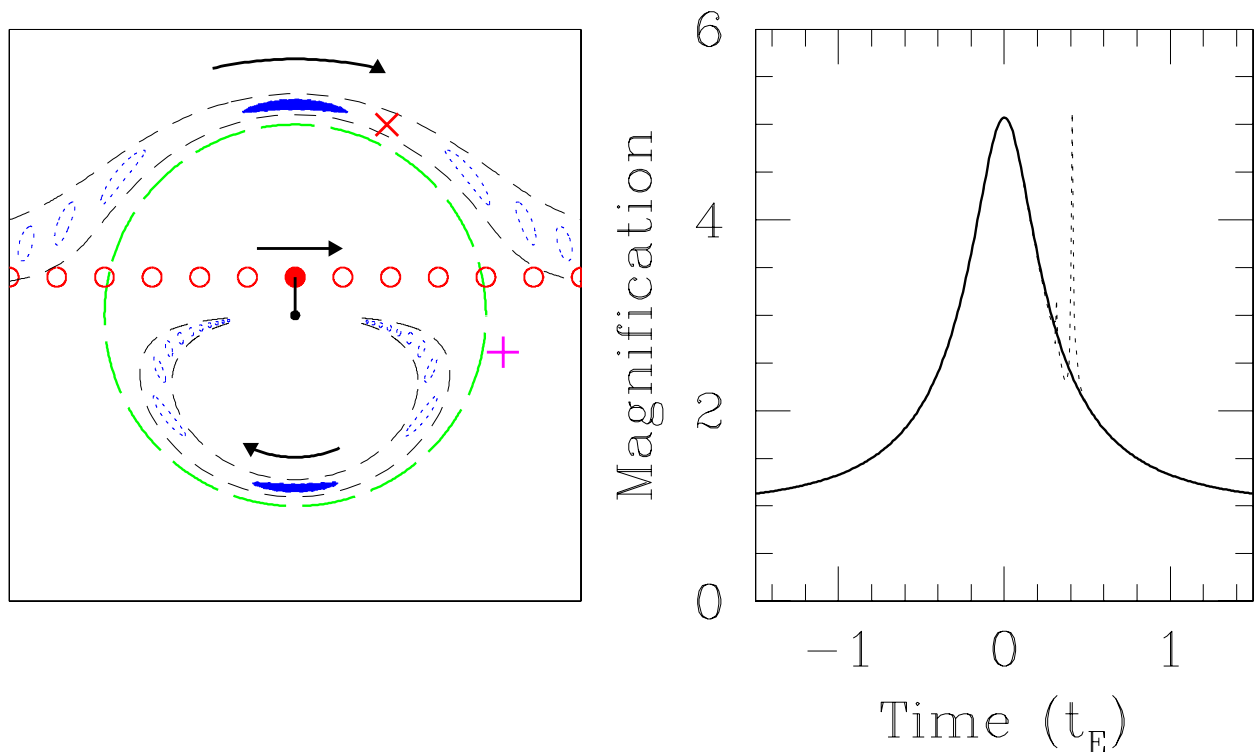


Figure 4: The left panel shows the images (dotted ovals) for several different positions of the source (solid circles) for a microlensing event with an impact parameter of 0.2 Einstein ring radii. The primary lens is indicated as a small black dot, and the primary lens Einstein ring is indicated a green long-dashed circle. If the primary lens happens to have a planet near the path of one of the images (roughly within the short-dashed lines), then the planet will perturb the light from the source, creating a deviation to the single lens light curve. Right: The magnification as a function of time is shown for the case of a single lens (solid) and accompanying planet (dotted) located at the position of the X in the left panel. If the planet was located at the + instead, then there would be no detectable perturbation, and the resulting light curve would be essentially identical to the solid curve.

perturb the light from the source associated with the image, creating a short-lived deviation from the single-lens form (Mao & Paczynski 1991; Gould & Loeb 1992).

Unfortunately, there are no simple analytic expressions relating the observable features of planetary perturbations to the underlying physical parameters of the planet and host star. Adding another body to the lens system increases the complexity of the lensing behavior significantly, and in particular inverting the lens equation for a binary lens to obtain the image positions for a given source position cannot be done analytically. Furthermore, the binary gravitational lens has a rich and complex phenomenology, which we will not attempt to explore in this brief review. We refer the reader to more comprehensive summaries by (Bennett 2008; Gaudi 2012). Here we will simply provide a qualitative discussion of planet detection with microlensing.

Three additional parameters are required to uniquely specify the light curve due to a binary lens (of which star/planet lenses are a subset). The planet/star mass ratio $q = M_p/M_*$ and instantaneous projected separation $s = r_\perp/r_E$ between the planet and star in units of r_E at the time of the event together specify the magnification structure of the lens, i.e., the magnification as a function of the (vector) source position $\mathbf{u} \equiv \boldsymbol{\beta}/\theta_E$. Finally, the parameter α (not to be confused with the phase angle) describes the orientation of the source trajectory relative to the projected planet/star axis. Thus a total of six parameters ($t_E, t_0, u_0, q, s, \alpha$) describe the magnification as a function of time for a binary lens and are thus generically observable.

Single lens microlensing events yield only one parameter that depends on the physical properties of the lens star, namely the time scale t_E . The time scale provides only a weak constraint on the lens mass, because it depends not only on the mass, but also on the lens and source distances, and the relative lens-source proper motion, all of which are relatively broadly distributed for a typical microlensing survey. In addition, the lens stars are typically quite faint and are blended with other stars (including the lensed source). Thus little is generally known about the host star properties. Planetary microlensing events generally yield two parameters that are related to the planet properties, q and s . While q is of interest in its own right, s is generally not, because it depends on the phase, orientation, and eccentricity of the orbit, as well as on the Einstein ring radius, all of which are a priori unknown. Therefore, s is only weakly correlated with the semimajor axis of the orbit, and provides essentially no constraint on the other orbital elements.

Although this “baseline” situation sounds quite dire, in fact it has been shown that with additional effort, it is possible to obtain substantially more information about the host star, planet, and its orbit for the majority of detected systems using a combination of subtle, higher-order effects that are detectable in precise microlensing light curves, and follow-up high-resolution imaging in order to isolate the light from the lens (Bennett et al. 2007).

1.7 Timing

A star or stellar remnant that exhibits regular, periodic photometric variability, such as pulsars, pulsating white dwarfs, eclipsing binary stars, pulsating hot subdwarfs, or even stars with transiting planets, can show evidence of a planetary companion through timing variations in those periodic phenomena. There are three principle sources of such variations: the Doppler shift, light travel time, and gravitational perturbations.

The first of these sources is exactly analogous to the radial velocity method, but measures

changes in frequencies of some property other than photons. If the period of the pulsations or eclipses can be measured to sufficient precision, then the interpretation of those variations is identical to that in the radial velocity method.

The light travel time effect comes about when the reflex orbit of a star about the center of mass of the star-planet system is sufficiently large that the additional light travel time across this orbit is detectable as a timing variation. This is not a truly distinct phenomenon from the Doppler shift timing method, since it is essentially the accumulated effects of the Doppler-shifted period that produce the timing anomaly. Depending on the period of the intrinsic variation and the physical size of the star’s reflex orbit, either effect, or both, may be detectable.

The above methods have been most successfully employed with pulsars (through the pulse arrival times) and eclipsing binary systems (through the timing of eclipse ingress and egress), and was responsible for the detection of the first exoplanets (Wolszczan & Frail 1992).

Finally, in the case of an eclipsing system, such as an eclipsing binary or a transiting planet, additional bodies in the system will perturb the orbits of the eclipsing bodies. These perturbations can be especially large if the perturbing body is near a mean motion resonance with the other bodies. When applied to systems of transiting planets this method is called *transit timing variations* (TTVs, Agol et al. 2005; Steffen & Agol 2005; Holman & Murray 2005), and has been most successfully employed by *Kepler* (e.g., Ford et al. 2012).

2 The Magnitude of the Problem

By almost any physical measure, planets are small in comparison to their parent stars, and the observable phenomena that are used to directly or indirectly detect them are likewise small. In this section, we attempt (where possible) to provide order-of-magnitude estimates of the precisions of the relevant observations that are required to detect planets using various methods. We then use these estimates, along with additional requirements imposed by the specifics of the detection method (i.e., the detection efficiencies), to provide a broad outline of the practical requirements that must be met for planet surveys to successfully detect planets with a given set of properties.

In general, specifying the criteria needed to detect a planet requires a detailed analysis of the signal and data properties, as well as a quantitative definition of the meaning of a detection. However, for many of the detection methods, a rough estimate can be obtained by decomposing the primary observable signal into two conceptually different contributions: an overall scale and detailed signal waveform. The overall scale, which depends on the physical parameters of the system, encodes the order-of-magnitude of the signal and largely dictates its detectability. The waveform itself depends on more subtle details of the system (i.e., the precise shape of the planet orbit), but typically takes on values of order unity and thus has a relatively small effect on the detectability of the signal. Therefore, in most cases, these two contributions can be fairly cleanly separated. In this approximation, the detectability of a planet with a given set of properties therefore primarily depends primarily on the overall signal scale, and the data quality and quantity, i.e., the typical observational uncertainties and the total number of observations. With this in mind, given a signal amplitude A , number of observations N , and typical measurement uncertainty σ , the detectability will

depend primarily on the total signal-to-noise ratio S/N , which scales as,

$$S/N \simeq g\sqrt{N}\frac{A}{\sigma} \quad (44)$$

where g is a factor of order unity that depends on the details of the signal.

2.1 Radial Velocities

The differential radial velocity signal of a planet has the form $\Delta V_r = KF(t; e, \omega_*, T_0, P)$, where $F(t)$ encodes the detailed shape of the RV signal. Assuming uniform and dense sampling of the RV curve over a time span that is long compared to P , and assuming a total of N observations each with measurement uncertainty σ_{RV} , the total signal-to-noise ratio is

$$(S/N)_{RV} \simeq g(e, \omega_*)\sqrt{N}\frac{K}{\sigma_{RV}}. \quad (45)$$

For a circular orbit, $g = 2^{-1/2}$, and is generally a weak function of e for $e \lesssim 0.6$. For larger eccentricities, g declines gradually, but more importantly the stochastic effects of finite sampling become significant for typical values of N (e.g., O'Toole et al. 2009; Cumming 2004). For planets with periods larger than the duration of the observations, the detectability depends additionally on the period and phase of the planet, and generally decreases dramatically with increasing period, typically as $(S/N)_{RV} \propto P^{-1}$ (e.g., Eisner & Kulkarni 2001; Cumming 2004).

Thus, a robust detection of a planet via RV typically requires achieving radial velocity precisions of $\sigma_{RV} \ll KN^{1/2}$. For $M_p \ll M_*$, the semiamplitude K is,

$$K = \left(\frac{P}{2\pi G}\right)^{-1/3} \frac{M_p \sin i}{M_*^{2/3}} (1 - e^2)^{-1/2} \quad (46)$$

Thus to detect a true Jupiter analog (i.e. a Jupiter-mass planet in a 11.8 yr, circular orbit around a Solar-mass star), for which $K \simeq (12.5 \text{ m/s}) \sin i$, requires a few dozen observations with precisions of a few m/s. An RV precision of 3 m/s corresponds to a Doppler shift of $K/c \simeq 10^{-8}$. The motion induced by an Earth analog is smaller by a factor of $318/(11.8)^{1/3} \sim 100$, so requires an additional two orders of magnitude in precision.

Typically the centroid of stellar spectral lines at fixed equivalent width can be measured with a precision of $\propto \sigma_V^{3/2}/N_{\text{eff}}^{1/2}$, where σ_V is the effective velocity width of the spectral line and N_{eff} is the effective number of photons in the line (i.e., the equivalent width of the line times the photon rate per unit wavelength). Maximizing the precision requires that the lines are well-resolved, and thus that the instrumental velocity resolution is less than the intrinsic velocity width of the star. For reference, the typical width of a spectral feature in a slowly rotating star is of order a few km/s ($\sim 10^{-5}$), and thus resolving powers of ($R = \Delta\lambda/\lambda \sim 10^5$) are needed, comparable to the resolving power of a typical high-resolution astronomical echelle spectrograph. The velocity precision per line is generally insufficient to detect planetary companions, and thus averaging over many lines is required. The statistical signal-to-noise ratio requirements are quite stringent, and thus bright stars and/or large apertures are generally needed.

Because the velocity precisions needed to detect planetary companions are well below the intrinsic widths of the spectral lines and even below the velocity precisions that can be obtained for individual lines, getting close to the photon limit requires excellent control of systematics. One of the most severe requirements is that the wavelength calibration must be both more precise than the desired velocity precisions, and stable over many times the orbital period of the planet. For a Jupiter analog, this wavelength calibration must be at a level of better than 10^{-3} of a resolution element, and stable over the course of decades. Since the Earth's motion about the Sun imparts a periodic Doppler shift of order 30 km/s ($v/c = 10^{-4}$), this accuracy and precision must be maintained even as the spectral lines move annually by 10^4 times the measurement precision.

There are at least two proven² paths to surmounting this challenge: though precise instrumental calibration with an absorption cell (the iodine technique), and through instrumental ultra-stability (as exemplified by HARPS), both of which are briefly described in §§4.3.1–4.3.5.

2.2 Astrometry

The magnitude of the differential astrometric offset of a star at a distance d due to a planetary companion has the general form $\Delta\theta_* = \theta_* F(t; e, \omega_*, i, T_0, P)$, where the semi-amplitude of the astrometric offset for a circular, face-on orbit is,

$$\theta_* \equiv \frac{a M_p}{d M_*}, \quad (47)$$

and we have assumed $M_p \ll M_*$. Again assuming uniform and dense sampling of the astrometric curve over a time span that is long compared to P , and assuming a total of N observations each with measurement uncertainty σ_{AST} , the total signal-to-noise ratio is

$$(S/N)_{AST} \simeq g(e, \omega_*, i) \sqrt{N} \frac{\theta_*}{\sigma_{AST}}. \quad (48)$$

We note for simplicity we have assumed that each observation yields a given uncertainty σ_{AST} on the magnitude of the vector position of the star relative to some reference frame; in reality each of these measurements may require a separate measurement for each of the two orthogonal directions. For $e = 0$, $g(i) = [0.5(1 + \cos^2 i)]^{1/2}$. For more general cases, the behavior of g is qualitatively similar to that for radial velocity signals. For $e \neq 0$, g depends additionally on ω_* and e , but is a relatively weak function of e for $e \lesssim 0.6$. However, the effects of finite sampling start to become more important as e increases, particularly for low N . When P is greater than the span of observations, the detectability also depends on T_0 and P , generally decreasing rapidly with increasing period, also typically as P^{-1} .

The magnitude of the astrometric signal of a Jupiter analog orbiting a nearby solar-type star at a distance of $D \sim 20$ pc is $\theta_* \simeq 0.25$ mas, whereas for an Earth analog the astrometric wobble is over 1500 times smaller, or around $0.15 \mu\text{as}$. Thus astrometric precisions of order

²Another technique, externally dispersed interferometry (EDI Erskine & Ge 2000), has shown promise as a third path to precise velocimetry. It employs an interferometer in front of a spectrograph at modest resolution, generating a known, unresolved, sinusoidal transmission function, somewhat analogous to a gas cell's absorption properties. The phase of the beating of the stellar spectrum against this pattern is a measure of radial velocity.

a mas or a μas are needed to detect gas giants or terrestrial planets, respectively. Since astrometry is most sensitive to planets orbiting the nearest stars, which have typical proper motions of $\sim 10^3$ mas/yr and annual parallactic motion of $\sim 10^2$ mas, the target stars typically move by more 10^3 times the required measurement precision over the course of a year, and secularly at 10^5 times the measurement precision per decade.

The photon limit of an astrometric measurement of a star depends on the signal-to-noise ratio and width of the point spread function (PSF), and scales as $\sigma_{AST} \sim \text{FWHM}/\sqrt{N}$, where N is the total number of photons in the measurement. As mentioned previously, diffraction limited PSFs, $\text{FWHM} \sim \lambda/D$, where D is either the aperture of the telescope or the baseline of the interferometer. Baselines of $\lesssim 100\text{m}$ therefore yield single measurement precisions of $\lesssim 4\text{mas}$. Therefore, the astrometric detection of planets generally relies on the ability to achieve both nearly photon-limited performance when measuring the centroid of individual images, and the ability to average many individual measurements to improve the final precision. As is the case with RV, excellent control of systematics is therefore required. There are a number of ways to achieve this, depending on the nature of the observing setup (direct imaging, interferometry, etc.).

Interferometric methods in particular allow precisions below 1 mas from the ground around bright stars with good, nearby reference stars, putting astrometric exoplanet detection within reach. Much better control of systematics is in principle possible from space, and thus space-based interferometers should be able to achieve precisions of 1–10 μas , making them a potential route for the detection of nearby true Earth analogs (Unwin et al. 2008).

2.3 Imaging

The flux ratio of a planet (or planet/star contrast) at a given wavelength λ and epoch can be expressed as $f_\lambda = f_{0,\lambda}\Phi(\alpha)$, where $\Phi(\alpha)$ describes the phase curve, whose form depends on the properties of the planet atmosphere, and is a function of the phase angle α , which in turn depends on the measurement epoch and orbital elements e, ω_p, i, T_0, P . The phase curve typically takes on values $\lesssim 1$, and thus the magnitude of the reflected light signal is characterized by $f_{0,\lambda}$. This factor depends on the nature of the planetary emission, but for reflected light and thermal emission takes the form (see equations 26 and 27),

$$f_{0,\lambda} = A_{g,\lambda} \left(\frac{R_p}{a} \right)^2 \quad (\text{Reflected}), \quad f_{0,\lambda} \simeq \left(\frac{R_p}{R_*} \right)^2 \frac{T_p}{T_*} \quad (\text{Thermal}), \quad (49)$$

where the latter equality assumes observations on the Rayleigh-Jeans tail, which yields the largest flux ratio. Further, for thermal emission arising from reprocessed starlight,

$$f_{0,\lambda} \simeq \left(\frac{R_p}{R_*} \right)^2 \left(\frac{R_*}{a} \right)^{1/2} [f(1 - A_B)]^{1/4} \quad (\text{Thermal, Equilibrium}) \quad (50)$$

The signal-to-noise ratio with which a planet can be directly detected in N measurements is (Kasdin et al. 2003; Brown 2005; Agol 2007),

$$(\text{S/N})_{dir} \simeq g\sqrt{N} \frac{f_{0,\lambda}}{\sigma_{\text{eff}}}. \quad (51)$$

Here $g = [N^{-1} \sum_k \Phi(\alpha_k)^2]^{1/2}$ is the root-mean-square of the phase function values at the times k of the observations, and σ_{eff} is the average effective per-measurement photon noise uncertainty normalized to the total stellar flux. In the usual background-limited case, the primary contributions to the uncertainty are residual light from the stellar point spread function, and local and exo-zodiacal light. In the case where the scattered light from the star is dominant, $\sigma_{\text{eff}} \sim \sqrt{C/N_*}$ (Kasdin et al. 2003), where C is the contrast ratio between the intensity of the scattered light from the star in the wings of the point spread function relative to the peak, and N_* is the total number of photons collected from the star in the measurement.

In contrast to many radial velocity and astrometric surveys, direct imaging surveys are generally designed with the requirement that such that the target signal-to-noise ratio *per measurement* is $\gtrsim 1$ (Kasdin et al. 2003), and thus $N \sim 1$. Achieving a sufficient S/N per measurement then typically translates into a requirement that $C \lesssim f_{0,\lambda}$, i.e., the flux from the planet within a given aperture is larger than the local background from the stellar PSF in the same aperture.

Young (< 1 Gyr old), self-luminous planets can still be quite warm (1000–2000 K), even at arbitrarily large separations from their parent stars, making them in some sense the easiest targets for direct imaging surveys. For these temperatures and roughly Jupiter radii, the planet/star flux ratios are $f_{0,\lambda} \sim 10^{-4}$ – 10^{-6} at near-IR wavelengths, or $\Delta m \sim 10$ – 15 magnitudes. Purely in terms of overall brightness, young exoplanets are rather easily detectable with large telescopes at infrared wavelengths; the primary difficulty therefore lies in suppressing the residual starlight at the position of the planet in order to achieve the contrast ratios C needed to distinguishing the planetary light from the star’s.

Since the albedos of exoplanets at distances of $\gtrsim 0.1$ AU are typically expected to be of order unity, the flux ratio of a planet in reflected starlight is $f_{0,\lambda} \sim (R_p/a)^2$. For a Jupiter analog this is $\sim 10^{-8}$ or about 20 magnitudes, whereas for an Earth analog this is $\sim 10^{-9}$, or about 23 magnitudes. The bolometric thermal flux ratio of an exoplanet in equilibrium with the starlight will be of the same order of magnitude as the reflected light flux ratio, however the monochromatic thermal flux ratio may be substantially larger, since the planet is cooler and so its thermal emission will peak in the Rayleigh-Jeans tail of the stellar blackbody emission. For a Jupiter analog at $\sim 10\mu\text{m}$, $f_{0,\lambda} \sim 10^{-8}$, whereas for an Earth analog it is $f_{0,\lambda} \sim 10^{-7}$.

Achieving a given contrast ratio is generally more difficult for small angular separations from the host star, and becomes generally impossible closer than some minimum *inner working angle*, θ_{IWA} . Thus the angular separation $\Delta\theta = r_{\perp}/d$ is another important parameter that determines the detectability of planets by direct imaging. The probability distribution of the projected separation r_{\perp} given a value of a for random orbital phases and viewing geometries is generally sharply peaked at a . Thus the typical angular separation of a planet with $a = 5.2$ AU orbiting a star at 20 pc is $\sim a/d = 250$ mas, whereas it is 50 mas for $a = 1$ AU. The inner working angle typically scales as (and is generally similar to) the diffraction limit of telescope,

$$\theta_{\text{diff}} \sim \lambda/D \quad (52)$$

where D is the diameter of the telescope (or the most widely separated components of an interferometer). This corresponds to 60 mas at 2 microns on an 8m telescope. Thus, surveys for Earth analogs are generally only feasible for the nearest stars.

The detectability of a planet by direct imaging depends on a complicated interplay between many variables, including the semimajor axis and size of the planet, age and distance to the star, and wavelength capabilities of the imaging system. For example, for reflected light surveys, the orbital separation affects the detectability of the planet through the opposing effects of contrast and angular separation. As another example, while younger planets tend to be more luminous, younger stars are also less common and so typically more distant. Additional factors may also contribute to these interplays, such as the brightness of the exozodiacal light as a function of semimajor axis, and variations in the planetary atmospheric properties (e.g., albedo and absorption bands) as a function of semimajor axis, age, and surface gravity. Direct imaging surveys therefore need to be designed carefully in order to maximize the discovery space and so chance of success. Combined with the technical challenges associated with achieving the contrast ratios and inner working angles needed for planet detection briefly described below, it is clear that direct imaging is a generally expensive and challenging detection method. Nevertheless, the potential payoff is enormous, particularly when considering the goal of directly imaging Earth analogs.

The technical aspects of imaging exoplanets comprise surmounting three challenges: corraling starlight into a nearly diffraction-limited PSF (and away from the planet image); mechanically blocking the starlight before it can diffract into the planet image; and subtracting the remaining starlight at the position of the planet image on the detector to reveal the planet image beneath. These three challenges are most forcefully attacked using adaptive optics, coronagraphy, and various forms differential imaging, respectively.

Adaptive optics (AO) refers to controlling the wavefronts of the incoming starlight and planet-light, which ideally consist of parallel planes propagating toward the telescope. The atmosphere and telescope optics both introduce aberrations to this wavefront which result in a PSF that differs significantly from that which a theoretically perfect optical system would produce (for an unocculted circular aperture, this would be an Airy function). For most ground-based telescopes, the primary source of wavefront aberrations is the atmosphere. Adaptive optics use movable or deformable mirrors which can be rapidly actuated in response to measured atmospheric aberrations, usually at tens to thousands of Hertz. These systems dramatically reduce the effects of atmospheric blurring, and the best of them can collect most of a star’s light into the shape dictated by optical diffraction. This heightens the peak of faint sources and reduces noise from the star outside the diffraction limit.

The technique of blocking the light of a bright source to reveal faint surrounding features is called coronagraphy. A coronagraph uses a series of masks in an optical system to block, reorganize, or alter the phase of incoming light such that “on-axis” light from the star is almost entirely blocked or caused to destructively interfere, while “off-axis” light (for instance, from a nearby planet) is relatively unaffected. Because important aspects of this technique happen in the pupil plane, stellar photons can be distinguished from planetary photons and rejected before they arrive on the same pixels on the detector. The effect is to reduce the contamination from stellar photons at the detector position of the planet, enhancing its detectability outside of the diffraction limit. There has been a proliferation of coronagraph designs in recent years, but they share the common feature of reducing or controlling the nature of the diffraction of the light into the planet image.

Adaptive optics systems and coronagraphs are not perfect. Their limitations, the aberrations introduced by the telescope, and diffraction spikes and rings from the aperture can result in significant amounts of starlight outside of the diffraction limit. The most insidious

of these effects are the semi-static patterns of “speckles” from residual wavefront errors. Differential imaging is the process of precisely determining the PSF of the starlight and attempting to subtract it, leaving only the planet light to be detected. In principle, differential imaging is limited by the quality of the model PSF and the unavoidable photon noise in the residuals to that model. The reference image being subtracted can be determined from a reference star (RDI), or from the data themselves through angular modulation (ADI), spectral analysis (SDI), polarization analysis (PDI), or other some other method or combination of methods.

A conceptual cousin of coronagraphy is interferometry, which allows widely separated apertures to combine incoming light to form interference fringes whose amplitudes and phases are sensitive to the presence of faint, off-axis companions. Such work is common at radio wavelengths, and in the infrared can be especially profitable just inside of the traditional diffraction limit of the telescope. Two such techniques are aperture masking interferometry, where a single telescope pupil is divided into small sub-apertures and the light is combined at the focal plane, and nulling interferometry where light from two telescopes is combined such that the starlight undergoes destructive interference, while the planet light, incoming at a slightly different angle, interferes constructively.

2.4 Transits

The fractional change in the flux of a star when it is transited by a planetary companion has the form $\Delta F_*/F_* = -\delta F(t; R_p, M_*, R_*, a, i, e, \omega_p)$, where $\delta = k^2$ is the square of the planet/star radius ratio, and the function $F(t)$ describes the detailed shape of the transit curve, and also generally depends on the surface brightness profile of the star. In the case of circular orbits, no limb darkening, and $R_p \ll R_*$, the form for $F(t)$ can be approximated by a box car with a depth of unity and duration of $T = T_{eq}(1 - b^2)^{1/2}$, where T_{eq} and b are the equatorial crossing time and impact parameter, respectively, as defined in §1.5. The fraction of time the planet is in transit (the transit duty cycle) is then $f_{tr} = T/P$.

Transit surveys generally operate by obtaining many observations of the target stars over a given time span. Of course, in order to be detectable a planet must be favorably aligned such that it transits. The transit probability is roughly $P_{tr} \sim R_*/a$. Then, assuming uniform sampling over a time span that is long compared to P , the signal-to-noise ratio of the transit when folded about the correct planet period is,

$$(S/N)_{tr} \simeq \sqrt{N f_{tr}} \frac{\delta}{\sigma_{ph}} \quad (53)$$

where N is the total number of observations and σ_{ph} is the fractional photometric uncertainty. Therefore, the probability of detecting a given planet via transits can be roughly quantified by three characteristics of the planetary system that depend primarily on R_p , R_* , and a ,

$$\delta = \left(\frac{R_p}{R_*} \right)^2, \quad P_{tr} \sim \frac{R_*}{a}, \quad f_{tr} \sim \frac{P_{tr}}{\pi}, \quad (54)$$

For a typical hot Jupiter with $R_p \simeq R_J$ and $P \simeq 3$ days orbiting a solar-type star, the transit probability is $P_{tr} \sim 10\%$, the transit depth is $\delta \sim 1\%$, and the duty cycle is $f_{tr} \sim 3\%$. These parameters place Hot Jupiters well within the capabilities of ground-based surveys, although the requirements are not trivial. First, since Hot Jupiters are

only found around $\sim 0.5\%$ of solar-type stars (Gould et al. 2006), many thousands of stars must be surveyed to guarantee a transiting Hot Jupiter. Obtaining relative photometry at precisions of less than a few millimagnitudes for thousands of stars simultaneously from the ground is generally difficult, and thus ground-based transit surveys operate close to the limit where $\delta/\sigma_{ph} \sim 1$. Therefore, hundreds of epochs during transit are needed for robust detections, corresponding to many thousands of total measurements. Aliasing effects arising from the diurnal constraints make achieving the required number of points in transit more challenging. All of these requirements are most easily met with relatively small aperture, but very wide field-of-view telescopes (e.g., Pepper et al. 2003; Bakos et al. 2004; Pollacco et al. 2006; McCullough et al. 2005).

In fact, finding transiting planets in wide-field surveys has proven even more difficult than simply meeting these (already difficult) requirements. First, wide-field transit surveys must contend with a huge fraction of false positives in the form of grazing eclipsing binaries (EBs), eclipsing binaries blended with brighter stars, and more exotic variables. Furthermore, even those signals that are consistent with a Jupiter-sized transiting object can, in principle, be much more massive companions, since the radius of compact objects is essentially constant from the mass of Saturn through $\sim 0.1M_{\odot}$ (e.g. Burrows et al. 1997). Thus radial velocity follow-up is needed to eliminate these false positives. Finally, high-precision (few m/s) radial velocity follow-up is needed to precisely measure the planet mass. The most successful searches achieve reliably high photometric accuracy over large fields, and employ multiple sites with good longitudinal coverage, sophisticated and automated transit identification algorithms, and thorough follow-up campaigns that using multi-band photometry, multi-band astrometry (to rule out close, chance alignments of EBs and foreground stars), and radial velocity work. Further characterization of a transiting planet is most successfully done using photometry and high signal-to-noise ratio spectroscopy with larger ground and/or space telescopes.

The requirements for the detection of Earth analogs orbiting solar-type stars are especially challenging. In this case, the fractional transit depth is $\sim 10^{-4}$, the transit probability is $\sim 0.5\%$, and the duty cycle is $\sim 0.1\%$ (i.e., the planet transits for $T \lesssim 13$ hours once a year). The detection of transiting Earth analogs requires essentially continuous observations of hundreds of stars, and precisions of better than ~ 0.1 mmag for periods of several years. These requirements cannot be met from the ground, and require space-based photometric monitoring. Indeed, the *Kepler* mission was designed to detect such planets, achieving the required photometric precision to detect Earth-sized planets on tens of thousands of stars (Borucki et al. 2010, see also § 5.3.2).

Transiting planets can also be found via photometric follow-up of known radial velocity companions; indeed the first transiting planet was discovered in this way (Henry et al. 2000; Charbonneau et al. 2000). Here the challenges are somewhat different than the “traditional” method of discovering transiting planets through their photometric signature. First, the probability that a given radial velocity companion will also transit its parent star is low, $\lesssim 10\%$. Second, radial velocity searches have traditionally been limited to relatively bright stars, and so the total number of stars have targeted for precision RV searches is $\sim 10^3$, making the total yield of transiting planets from this sample also low. Furthermore, achieving photometry at the level of precision needed to detect the transit signature may be challenging for very bright stars, primarily because of the lack of suitable comparison stars. Finally, the uncertainties in the predicted times of inferior conjunction from the radial velocity fits can

be quite large, from several hours to several days. Nevertheless, seven transiting systems have been discovered amongst the sample of companions first discovered via radial velocity, and there are ongoing projects that aim to increase this sample by first refining the radial velocity ephemerides of promising systems, and then performing photometric follow-up (Kane et al. 2009).

2.5 Microlensing

Unlike the detection methods discussed above, the signals caused by planetary companions in microlensing events cannot be described analytically except in a few specific limits that are not generally applicable. Nevertheless, we can provide some qualitative guidelines and approximate scaling behaviors that will elucidate the general requirements for successful surveys for planets with microlensing. We stress that, because of the large diversity in the properties of the systems that give rise to gravitational microlensing events, the expressions provided should be treated as very rough estimates only.

A somewhat unusual attribute of the microlensing method is that the magnitude of a microlensing perturbation does not depend on the properties of the planet in the general case. Rather, the magnitude depends primarily on the angular separation of the planet from the image(s) it is perturbing. However, the duration of the planetary perturbation does depend on the planet properties, in particular the mass ratio q . Very approximately, the duration of the planetary deviation is $\Delta t_p \sim q^{1/2} t_E$, where t_E is the primary event time scale. The primary event light curves must be sampled on a time scale significantly smaller than Δt_p in order to detect and characterize the planetary perturbation. Furthermore, the detection probability also depends on the planet mass ratio, such that $P_{det} \sim 20\% (q/0.001)^{5/8}$ (Horne et al. 2009). This detection probability is averaged over a uniform distribution of impact parameters, and is appropriate for planets with projected separations that are within a factor of ~ 2.6 of the Einstein ring radius, $r_\perp \sim [0.6 - 1.6] d\theta_E$, sometimes called the “lensing zone”. Planets with separations much smaller or much larger than this range have substantially lower probability of detection. As discussed in the context of direct imaging, the distribution of projected separation r_\perp for random viewing geometries and orbital phase is sharply peaked at $r_\perp \sim a$.

In addition, there is a minimum mass that can be detected in microlensing surveys, that is set by the finite size of the source stars. When the angular size of the planet perturbation region is substantially smaller than the angular size of the source, the planet perturbs only a small fraction of the source, and the magnitude of the resulting deviation is strongly suppressed. A rough limit on the mass ratio can be established by when the angular size of the source θ_* is a factor of ~ 3 times larger than the angular Einstein ring radius of the planet $\theta_p = q^{1/2} \theta_E$, corresponding to roughly an order of magnitude suppression of the planet signal. Thus $q_{min} \sim 0.1 \rho_*^2$, where $\rho_* \equiv \theta_*/\theta_E$ (Gould & Gaucheron 1997).

Thus the parameters that determine the detectability of planets with microlensing are

$$\Delta t_p \sim \left(\frac{M_p}{M_*} \right)^{1/2} t_E, \quad P_{det} \sim 20\% \left(\frac{M_p/M_*}{0.001} \right)^{5/8}, \quad a \sim [0.6 - 1.6] d\theta_E, \quad q_{min} \sim 0.1 \rho_*^2, \quad (55)$$

where the parameters t_E , and ρ_* additionally depend on the mass and distance to the host star via the angular Einstein ring radius (see Eq. 38). The distributions of M_* , t_E , d , and θ_E for

microlensing events toward the Galactic bulge are quite broad, but we can take typical values of $M_* \simeq 0.5 M_\odot$, $t_E \simeq 25$ days, $d \sim 4$ kpc, and $\theta_E \sim 0.7$ mas. Thus microlensing planet surveys are most sensitive to planets with semimajor axes of $a \simeq [1 - 5] \text{ AU} (M/0.5 M_\odot)^{1/2}$. For a Jupiter-mass planet, the typical planet perturbation duration is $\Delta t_p \sim 1$ day, and the typical detection probability is $\sim 30\%$ in the lensing zone. For an Earth-mass planet, $\Delta t_p \sim 1.5$ hours, whereas the detection probability in the lensing zone is $\sim 1\%$.

The typical dimensionless source size for a clump giant star ($\sim 13 R_\odot$) in the Galactic bulge is $\rho_* \sim 0.01$, whereas for a turn-off star ($\sim R_\odot$) it is ~ 0.001 . Thus the minimum mass ratio that can be detected by monitoring clump giant sources is $q_{min} \sim 10^{-5}$, corresponding to $\sim 1.7 \times$ mass of the Earth for a typical primary lens of $0.5 M_\odot$. For main sequence stars in the bulge, $q_{min} \sim 10^{-7}$, corresponding to just over the mass of the Moon! Thus detecting planets with mass of the Earth or less requires monitoring main-sequence stars. The difficulty lies in the fact, in the crowded fields toward the Galactic bulge, most main sequence stars are severely blended with other unrelated background stars in typical ground-based seeing conditions, dramatically increasing the photometric noise. Therefore, detecting planets with mass substantially less than that of the Earth generally requires a space-based survey (Bennett & Rhie 2002; Bennett 2008).

A final difficulty with in microlensing surveys is the low overall event rate of gravitational microlensing events. Toward the Galactic bulge, the rate of microlensing events is roughly $\Gamma \sim 10^{-5}$ per star per year (e.g., Kiraga & Paczynski 1994). Thus, in order to detect $\sim 10^3$ events per year (the current number of microlensing events that are detected per year toward the Galactic bulge by the Optical Gravitational Lensing Experiment (OGLE) collaboration³), of order 100 million source stars must be monitored. There are 3 million stars per square degree down to an I magnitude of 19 in Baade’s window (Holtzman et al. 1998), where $I \sim 19$ is roughly the peak of the distribution of baseline magnitude for microlensing events. Thus several tens of square degrees of the bulge must be monitored.

The unpredictability of microlensing events requires monitoring the potential source stars with a cadence that is substantially smaller than the timescale of interest. For the primary microlensing events, which have a typical $t_E \sim 25$ days, this means roughly daily observations. Detecting the planetary perturbations on these events requires much higher cadences of a few hours or less. Furthermore, since the total durations of the planetary perturbations are of order a day or less, networks of longitudinally-distributed telescopes must be employed in order to avoid missing part or all of the perturbations. Given these requirements, traditional microlensing planet surveys have used a two-tier approach, where collaborations with dedicated access to telescopes with a relatively wide fields of view of $\sim 0.5 - 2$ square degrees monitor the tens of square degrees needed to detect the primary microlensing events, but with cadences that are generally insufficient to detect planetary perturbations on these events (Udalski 2003; Sako et al. 2008). These survey collaborations alert the microlensing events real-time before the peak magnification, thus allowing “follow-up” collaborations with access to narrow-angle telescopes on several continents to monitor only a subset of the stars that display ongoing microlensing events with the cadences needed to detect planetary perturbations (Albrow et al. 1998; Tsapras et al. 2009; Dominik et al. 2010; Gould et al. 2010). Future surveys will operate on a very different principle, as described in §5.3.3.

³See <http://ogle.astrouw.edu.pl/ogle4/ews/ews.html>.

2.6 Timing

The magnitude of the signal in other planet detection techniques varies. Timing for millisecond pulsars like PSR 1257+12 can in principle detect extremely low mass objects (significantly $< 1M_{\oplus}$) given a sufficient amount of data, limited primarily by pulsar timing noise.

Other timing techniques, such as eclipsing binary times or pulsating hot subdwarfs, rely on timing variations being correctly interpreted as a light-travel time effect of a star or stellar system orbiting a common center of mass with an unseen companion. A summary of such detections is listed in Schuh (2010); most of these detections imply minimum companion masses of several times that of Jupiter. The sensitivities of these methods is difficult to determine, however, since they depend on the magnitude of all non-orbital origins in timing variations, which have not been well quantified. Most of the current detections are of fewer than two full apparent orbits (periods are 3–16 yr) and so the strict periodicity that is characteristic of Keplerian signals cannot yet be confirmed. Further, quasi-cyclical timing variations may be generated by poorly understood internal mechanisms such as the “Applegate effect” (Applegate 1992). Following these apparent planetary systems for multiple orbits will help illuminate the true sensitivities of these methods.

Transit timing variations (TTVs) provide an extremely sensitive method of detecting new planets or characterizing known planets in a transiting system. The sensitivity is a complex function of the orbital parameters of the planets involved, but is optimized when the planets are in mean-motion resonances (Veras et al. 2011). *Kepler* is sufficiently precise in its timing to measure variations of order minutes in the ingress and egress times of transiting planets, which in principle allows it to reach mass precisions of order $1 M_{\oplus}$ over several years of observation.

In known multi-transit systems, these variations can be used to infer the masses of the planets involved (e.g. Lissauer et al. 2011) and in apparently single systems they can be used to detect non-transiting planets (e.g. Ballard et al. 2011). Ground-based planet transit timing will generally be limited to precisions of a tens of minutes, and so have correspondingly weaker sensitivities.

3 Comparisons of the Methods

In the previous sections, we reviewed the primary exoplanet detection methods in some detail, outlining the principles of each method, including the primary physical observables and practical challenges associated with achieving robust detections. In this section, we place these discussions in the context of the larger goal of constraining exoplanet demographics by outlining the regions of planet and host star parameter space where each method is most sensitive. We then compare the methods with one another in this context, highlighting the strong complementarity of the methods. We also briefly discuss and compare how the intrinsic sensitivity of each method to planets in the Habitable Zones of their parent stars scales with host star mass.

The sensitivity of the various detection methods as a function of planet mass and separation is illustrated in Figure 5. We show the masses and semimajor axes of the exoplanets discovered by radial velocities, direct imaging, timing, transits, and microlensing, as of Dec.

2011. In addition, we show estimates of the sensitivity of various surveys using radial velocities, direct imaging, transits, microlensing, and astrometry. In the following subsection, we explain the scaling of these survey sensitivities with planet parameters, and explain our specific choice for their normalization. Host star mass is a third parameter that can strongly influence the sensitivity of these methods, but is suppressed in this figure. Therefore, in order to provide a somewhat fairer comparison across the broad range of host star masses represented in this figure, we normalize the semimajor axis by an estimate of the snow line distance (e.g., Kennedy & Kenyon 2008),

$$a_{sl} = 2.7 \text{ AU} \frac{M_*}{M_{\odot}}. \quad (56)$$

The snow line is the location in the protoplanetary disk where the temperature is below the sublimation temperature of water. In the currently-favored paradigm of planet formation, the snow line distance plays an important role, as the larger surface density of solids beyond the snow line facilitates giant planet formation, whereas primarily rocky planets are expected to form interior to the snow line (e.g., Lissauer 1987; Pollack et al. 1996; Ida & Lin 2004; Mordasini et al. 2009).

Both the locations of the known planets and the regions of sensitivity in Figure 5 serve to illustrate the complementarity of the various detection methods. In particular, radial velocity and transit surveys are most sensitive to relatively short-period exoplanets with separations interior to the snow line. State of the art surveys using these methods are sensitive to planets as small as the Earth. In contrast, direct imaging and microlensing surveys are most sensitive to planets beyond the snow line. Current direct imaging surveys are sensitive to very widely-separated, massive planets. Current and near-term microlensing surveys are sensitive to planets with masses greater than that of the Earth, whereas a space-based microlensing survey would be sensitive to planets with mass greater than that of Mars and separations greater than a few AU, including free-floating planets. The combined sensitivity of current and proposed surveys using the methods discussed in the chapter encompasses an extremely broad volume of parameter space, including planets with masses greater than that of the Earth for arbitrary separations (including free-floating planets), host stars with masses from the bottom of main sequence to several times the mass of the sun, and distances from the solar neighborhood to the Galactic center. Thus the full complement of these methods can potentially provide a nearly complete picture of the demographics of exoplanets.

3.1 Sensitivities of the Methods

- **Radial Velocities.** The radial velocity signal and signal-to-noise ratio scales as

$$(S/N)_{RV} \propto M_p P^{-1/3} M_*^{-2/3} \propto M_p a^{-1/2} M_*^{-1/2}. \quad (57)$$

Thus, at fixed host star mass, RV surveys are generally more sensitive to more massive planets, and have a weak preference for shorter-period planets, at least for periods shorter than the span of the measurements. At fixed S/N, the minimum detectable mass scales as $M_{p,min} \propto P^{1/3} M_*^{2/3} \propto a^{1/2} M_*^{1/2}$. This mass limit is shown in Figure 5 assuming $M_* = M_{\odot}$ and a minimum detectable RV signal of $K \sim 1$ m/s (i.e., corresponding to a $(S/N)_{RV} \sim 10$ detection with 100 observations each with single

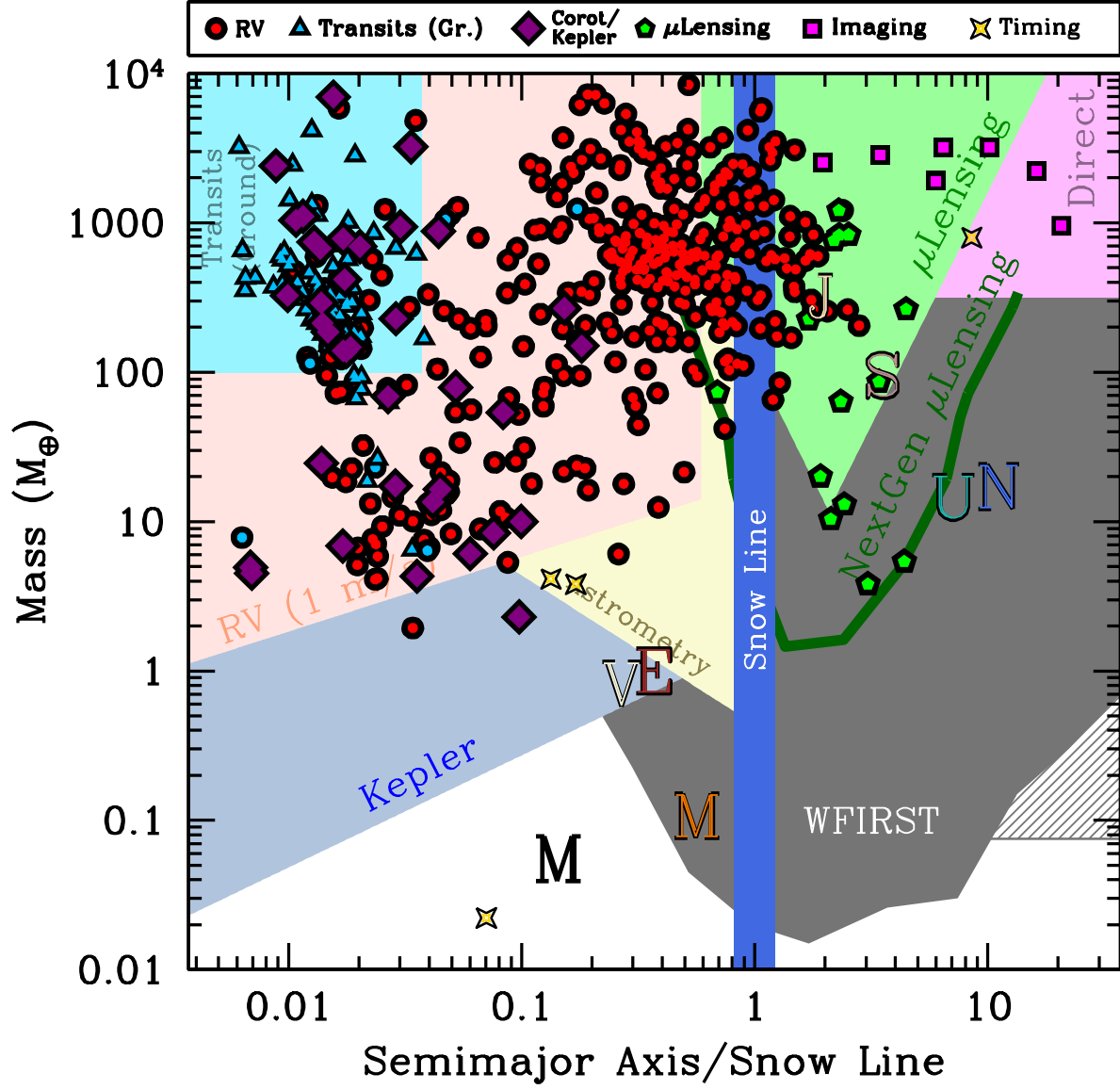


Figure 5: The points show the masses versus semimajor axis in units of the snow line distance for the exoplanets that have been discovered by various methods as of Dec. 2011. See the Extrasolar Planets Encyclopedia (<http://exoplanet.eu/>) and the Exoplanet Data Explorer (<http://exoplanets.org/>). Here we have taken the snow line distance to be $a_{sl} = 2.7 \text{ AU}(M_*/M_\odot)$. Radial velocity detections (here what is actually plotted is $M_p \sin i$) are indicated by red circles (blue for those also known to be transiting), transit detections are indicated by blue triangles if detected from the ground and as purple diamonds if detected from space, microlensing detections are indicated by green pentagons, direct detections are indicated by magenta squares, and detections from pulsar timing are indicated by yellow stars. The letters indicate the locations of the Solar System planets. The shaded regions show rough estimates of the sensitivity of various surveys using various methods, demonstrating their complementarity.

measurement precisions of $\sim 1\text{m/s.}$). In principle, sufficiently massive planets can be detected even when they have periods longer than the duration of observations, however it will generally not be possible to uniquely measure $M_p \sin i$ and P in these cases, and thus the usefulness of such ‘detections’ are significantly compromised. Therefore, we simply assume an upper limit on the period of $P = 2000$ days.

At fixed planet properties, the RV signal increases with decreasing host star masses as $M_*^{-2/3}$. However, there are many additional factors that enter into the overall detectability as a function of mass, through the radial velocity uncertainty σ_{RV} . At fixed distance to the host star, the velocity uncertainty due to photon noise increases with decreasing mass for main-sequence stars, both because of the strong mass-bolometric luminosity relation for main-sequence stars, and because of the difficulties of continuum normalization in very cool stars, where most RV surveys are carried out. The intrinsic velocity information in stellar spectra also varies as a function of spectral type. In particular hot ($T_{\text{eff}} \gtrsim 6500\text{K}$) stars have few spectral lines and typically rotate much more rapidly than cooler stars with convective envelopes. Finally, the astrophysical radial velocity noise (i.e., “jitter” due to spots) also depends on spectral type and stellar age (Wright 2005). When taken together, these factors tend to favor late G or early K quiet main-sequence stars as the most promising for detecting low-mass planets (e.g., Pepe et al. 2011).

- **Astrometry.** The astrometric signal and signal-to-noise ratio scales as

$$(S/N)_{AST} \propto M_p P^{2/3} M_*^{-2/3} d^{-1} \propto M_p a M_*^{-1} d^{-1}, \quad (58)$$

and so at fixed stellar mass, astrometric surveys are more sensitive to massive, long-period planets. At fixed S/N, the minimum detectable mass scales as $M_{p,min} \propto P^{-2/3} M_*^{2/3} d \propto a^{-1} M_* d$. This limit is shown in Figure 5 assuming $M_* = M_\odot$ and $d = 10$ pc, and a minimum detectable astrometric signal $\theta_* \simeq 0.35 \mu\text{as}$ (i.e., a $(S/N)_{AST} \sim 5$ detection with 200 2-D observations each with $\sigma_{AST} \sim 1 \mu\text{as}$ precision). As with radial velocity observations, although it is possible to detect the astrometric signal of planets with period larger than the duration of observations, it is generally not possible to independently measure the mass and orbital parameters with observations that do not cover a complete orbit. This is particularly problematic for astrometric observations, because in this regime the signal of the proper motion of the star is partially degenerate with the astrometric signal of the planetary companion. Astrometric surveys are therefore expected to have the most sensitivity to planets with periods similar to the survey duration, and increasing the survey duration has a strong effect on the survey yield.

At fixed planet properties and host star distance, the astrometric signal increases with decreasing host star mass as $M_*^{-2/3}$. Stellar spots are generally not expected to be an important source of astrometric noise (Makarov et al. 2009), and thus the only additional dependence of the sensitivity of astrometric surveys on stellar mass enters through the effects of the typical distance and photon noise uncertainty of the host stars. Specifically, low-mass stars are more common and thus have a smaller typical distance, but are less luminous and thus yield poorer astrometric precision.

- **Imaging.**

For direct detection in reflected and equilibrium thermal emission light, the planet/star flux ratio and thus the signal-to-noise ratio scales as

$$(S/N)_{dir} \propto R_p^2 a^{-2} \quad (\text{Reflected}), \quad (59)$$

$$(S/N)_{dir} \propto R_p^2 T_p R_*^{-2} T_*^{-1} \quad (\text{Thermal}) \quad (60)$$

$$(S/N)_{dir} \propto R_p^2 R_*^{-3/2} a^{-1/2} \quad (\text{Thermal, Equilibrium}), \quad (61)$$

where the last two forms again assume observations in the Rayleigh-Jeans tail. The other primary requirement for direct imaging is that the angular separation between the planet and star is larger than inner working angle, and thus $a \gtrsim \theta_{IWA} d^{-1}$. Thus at fixed primary properties and distance, larger and hotter planets are more readily detectable. As discussed in §2.3, the dependence of detectability on semimajor axis is not trivial: planets with larger orbits generally have smaller flux ratios, however they must have an angular separation greater than the inner working angle to be detectable. Furthermore, additional effects that are likely to depend on the planet semimajor axis may affect the detectability, such as the variation of the planetary albedo with separation.

At fixed planet properties, the signal-to-noise ratio with which a planet can be detected in reflected light is largely independent of the host star properties. For detection in thermal emission, larger and/or hotter host stars generally give rise to smaller flux ratios. The other effect of host star mass enters through the dependence on distance: less massive host stars are more numerous and so have a smaller average distance, whereas more massive host stars are more luminous and thus give rise to smaller photon noise uncertainties at fixed distance. Finally, the age of the host star plays an important role in the detectability of planets, particularly with current surveys: young, self-luminous planets have flux ratios that are both larger than would be expected for planets whose emission is dominated by reflected light or equilibrium thermal emission, and are independent of their semimajor axis. Thus relatively luminous planets with separations well beyond the inner working angle can be found around young stars.

Current ground-based imaging surveys are most sensitive to young, massive ($M_p \gtrsim M_{JUP}$) self-luminous planets with semimajor axes of $\gtrsim 10$ AU around the nearest stars. Thus these surveys are sensitive to planets in a regime of parameter space that is not currently being probed by other methods. We illustrate the current region of sensitivity of imaging surveys in Figure 5, assuming planets with $M_p \gtrsim M_{JUP}$ and $a \gtrsim 10$ AU can be detected. Future surveys (some of which will be initiated very soon) will be sensitive to a much broader region of planet parameter space.

- **Transits** Assuming uniformly-sampled observations over a time span T that is long compared to the planet period, the signal-to-noise ratio with which a transiting planet can be detected scales as

$$(S/N)_{tr} \propto R_p^2 P^{-1/3} M_*^{-5/3} \propto R_p^2 a^{-1/2} M_*^{-3/2}, \quad (62)$$

where we have assumed $R_* \propto M_*$, as appropriate for stars on the main sequence with $M \lesssim M_\odot$. In addition, the transit probability scales as $P_{tr} \propto P^{-2/3} M_*^{2/3} \propto$

$a^{-1}M_*$, and the requirement to detect at least n transits sets a strict lower limit on the period $P \leq T/n$. Thus for fixed host star properties, the sensitivity of transit surveys is strongly weighted toward short period, large-radius planets. At fixed S/N, the minimum detectable planet radius scales as $R_{p,min} \propto P^{1/6} M_*^{5/6} \propto a^{1/4} M_*^{3/4}$. For planets with a constant density, this translates into a minimum mass of $M_{p,min} \propto R_{p,min}^3 \propto P^{1/2} M_*^{5/2} \propto a^{3/4} M_*^{9/4}$. This limit is shown in Figure 5, assuming a minimum $(S/N)_{tr} = 8$ and a mid-latitude transit and photon noise-limited precision for a $M_* = M_\odot$, $V = 12$ star from *Kepler* (Gilliland et al. 2011). The relatively strong dependence of the signal-to-noise ratio on planet radius, combined with the decreasing transit probability with increasing planet period, generally implies that the yield of a transit survey is a relatively weak function of the total duration T .

Main-sequence stars are clearly the best targets for transit searches. At fixed planet radius and period, low-mass main-sequence stars yield larger transit signals. However, for photon noise limited uncertainties, the signal-to-noise ratio also depends on the stellar luminosity in the wavelength of the observations, and the distance to the star. Low-mass stars are more common, and are therefore are closer on average. These net result of these various countervailing effects on the scaling of the sensitivity of transit surveys with host star mass depends on the survey parameters, particularly the wavelength, target field, and magnitude limit (Pepper & Gaudi 2005). All-sky surveys in the visual at fairly bright magnitudes tend to be dominated by F and G stars (Pepper et al. 2003), but surveys for fainter stars, or surveys in near-IR wavelengths, tend to be more heavily weighted to toward low-mass stars.

• Microlensing

As discussed previously, microlensing surveys are less amenable to analytic characterization of the sensitivity and scaling with planet and host star parameters. Nevertheless, we have the general qualitative result that the sensitivity peaks for semimajor axes that are similar to the Einstein ring of the host star lens, $a_{opt} \sim 2.85 \text{ AU} (M_*/0.5M_\odot)^{1/2}$. Both the detection probability at fixed semimajor axis and range of sensitivity around this peak increases for larger mass ratio. The range of planet mass and semimajor axis to which a given microlensing survey is most sensitive depends on the details of the survey design, in particular the number and peak magnification of the primary events that are monitored, and the precision and cadence of the observations. In Figure 5, we show representative estimates for the sensitivity of a current ground-based microlensing survey based on the analysis of Gould et al. (2010), a next-generation ground-based survey as described in §5.3.3, and a space-based survey similar to WFIRST as described Green et al. (2011). Generally, current microlensing surveys are most sensitive to planets with $M_p \gtrsim 10 M_\oplus$, with separations just beyond the snow line spanning a factor of a few in semimajor axis. Next generation ground-based surveys will lower the sensitivity in mass by roughly an order of magnitude to $M_p \gtrsim M_\oplus$, and broaden the range of semimajor axis by a factor of ~ 2 . A space-based survey would be sensitive to planets with mass greater than the mass of Mars with separations greater than a few AU, including analogs to all of the solar system planets except Mercury.

Because microlensing does not rely on the detection of photons from the host star, the sensitivity of a microlensing survey to the host star parameters enters primarily through

the microlensing event rate as a function of host star mass. The microlensing event rate is given by the integral of the number density of lenses along the line of sight to the bulge, weighted by the cross section for lensing, which depends on the host star Einstein ring radius ($\propto M_*^{1/2}$) and its projected transverse velocity. Figure 6 shows a theoretical estimate of the microlensing event rate toward the Galactic bulge, as a function of the lens mass. The sensitivity of microlensing planet surveys is roughly proportional to this event rate. Thus microlensing surveys are sensitive to main-sequence hosts with mass from below the hydrogen burning limit up to the turn-off of the stellar population ($\sim M_\odot$), as well as remnant hosts. The sensitivity to brown dwarf and main-sequence hosts is roughly constant per $\log M_*$.

3.2 Habitable Planets

Of particular interest is the detection of terrestrial planets in the Habitable Zones of their parent stars. In §2, we discussed the magnitude of the signal expected for an Earthlike planet separated by one AU from a solar type star for various detection methods. These signals are generally quite small. However, we can and should also consider the signals and detectability of Earthlike planets orbiting in the Habitable Zones of main-sequence stars with mass significantly different than the sun. Because the masses, radii, and luminosities of stars on the main sequence can span an order of magnitude or more, both the location of the Habitable Zone and the magnitude of the signal expected from an Earthlike habitable planet can vary substantially.

In this subsection, we derive the scaling of the detectability of Earthlike habitable planets with host star mass. To this end, we adopt a power-law form for the stellar mass-bolometric luminosity relation,

$$\frac{L_*}{L_\odot} \sim \left(\frac{M_*}{M_\odot} \right)^4. \quad (63)$$

Our adopted exponent of 4 roughly corresponds to that found from a weighted fit to the data for benchmark binary systems analyzed in Torres et al. (2010). This form provides a reasonable approximation of this data set over the full span of masses of $\sim 0.2M_\odot - 50M_\odot$. We note, however, that there are significant deviations from this form within the range, particularly for stars below the fully-convective boundary, which are generally more luminous than predicted by Equation 63. Nevertheless, we will adopt this simple form for the purposes of illustration. With this adopted mass-luminosity relation, we can define the location of the Habitable Zone as,

$$a_{\text{HZ}} = \text{AU} \left(\frac{L_*}{L_\odot} \right)^{1/2} \sim \text{AU} \left(\frac{M_*}{M_\odot} \right)^2, \quad P_{\text{HZ}} \sim \text{yr} \left(\frac{M_*}{M_\odot} \right)^{5/2}, \quad (64)$$

Therefore, the Habitable Zone location ranges from a semimajor axis of $\sim 0.01\text{AU}$ and period of ~ 1 day for a star at the bottom of the main sequence to ~ 4 AU and ~ 6 years for a $M_* \sim 2 M_\odot$ star. We adopt a mass-radius relation of the form,

$$\frac{R_*}{R_\odot} \sim \frac{M_*}{M_\odot} \quad (65)$$

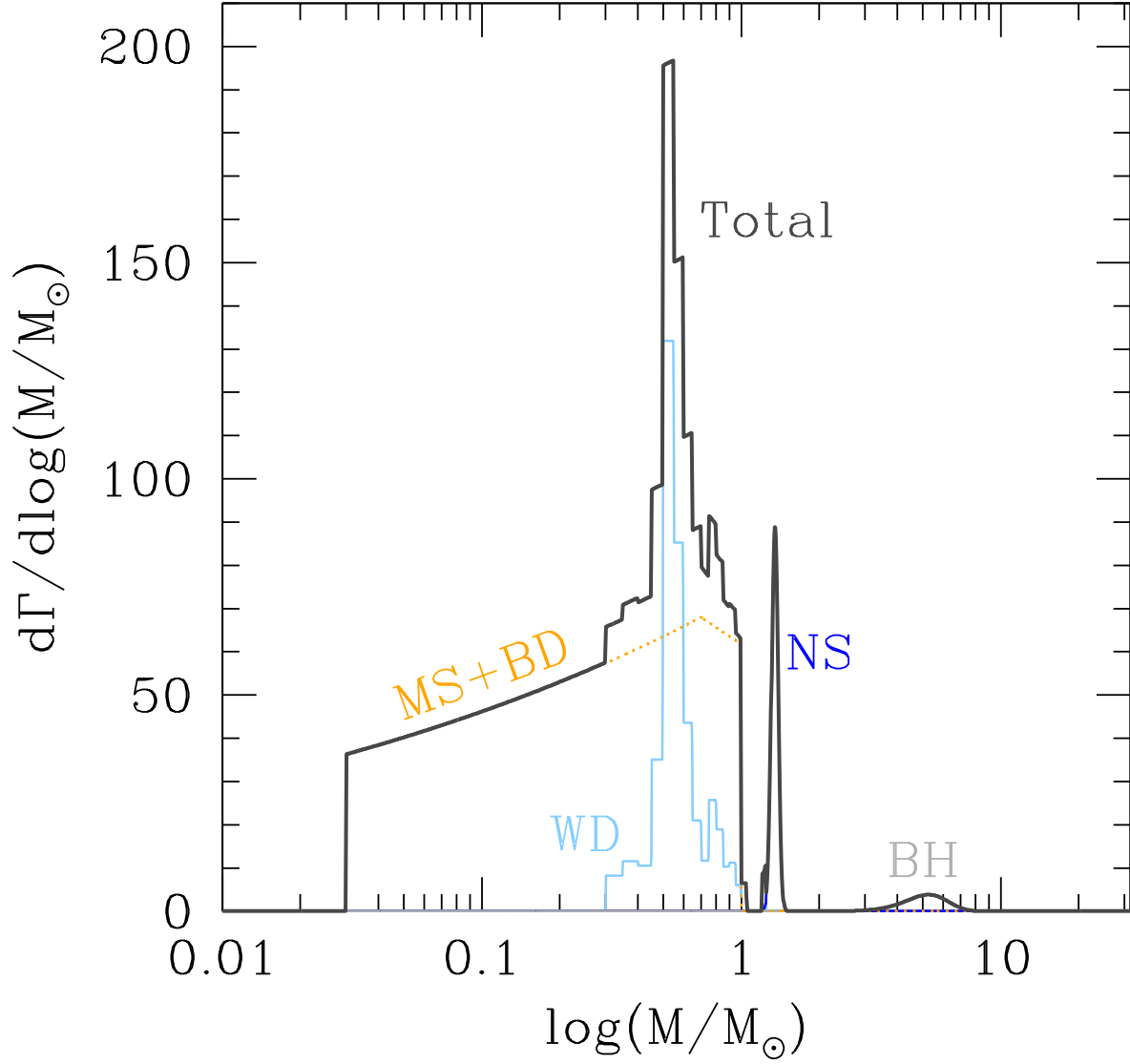


Figure 6: The solid black curve shows the theoretical estimate of total event rate of microlensing events toward the Galactic bulge from Gould (2000), as a function of the mass of the lens. This event rate is decomposed into its contribution from main-sequence and brown dwarf lenses, white dwarfs, neutron stars, and black holes, as indicated. The sensitivity of microlensing planet surveys is roughly proportional to this event rate. Adapted from Gould (2000), reproduced by permission of the AAS.

which describes the data in Torres et al. (2010) reasonably well for non-evolved stars with $M_* \lesssim 2M_\odot$.

With these assumptions, we can now use the results from §3.1 to derive the scaling of the signal of a habitable planet with host star mass for the various methods we have discussed.

- **Radial Velocities.** For radial velocity surveys, the radial velocity and signal-to-noise ratio for planets in the Habitable Zone scales as

$$(S/N)_{RV} \propto M_p M_*^{-3/2} \quad (\text{Habitable}). \quad (66)$$

Therefore, all else being equal, Habitable Zone planets are significantly easier to detect around lower-mass stars. In particular, for stars with $M \lesssim 0.2 M_\odot$, the radial velocity amplitude for an Earth-mass planet in the Habitable Zone is expected to be $\gtrsim 1\text{m/s}$, which is within the reach of current instrumentation (Bean et al. 2010).

- **Astrometry.** The astrometric signal and signal-to-noise ratio for habitable planets scales as,

$$(S/N)_{AST} \propto M_p M_* d^{-1} \quad (\text{Habitable}), \quad (67)$$

and thus at fixed distance and planet mass, astrometric surveys are more sensitive to habitable planets orbiting higher-mass stars, provided that the period of the planets is less than the duration of the survey. In addition, higher-mass stars are more luminous and thus have smaller photon noise uncertainties. On the other hand, higher-mass stars are also less common and thus are typically more distant. The net result of these factors is that A and F stars are the most promising targets for astrometric searches for planets in the Habitable Zones of nearby stars (Gould et al. 2003a).

- **Imaging.** For direct detection of habitable planets in thermal equilibrium with their host stars, the planet star flux ratio and signal-to-noise ratio scale as,

$$(S/N)_{dir} \propto R_p^2 M_*^{-4} \quad (\text{Reflected, Habitable}), \quad (68)$$

$$(S/N)_{dir} \propto R_p^2 M_*^{-5/2} \quad (\text{Thermal, Habitable}), \quad (69)$$

strongly favoring low-mass stars. Note that, by definition, the amount of stellar irradiation for a planet in the habitable zone is independent of the mass of host star, and thus for fixed planet properties the thermal or reflected flux of the planet is also independent of the mass of the host star. The dependence on stellar mass in the above scaling relations therefore arises simply from the change in the flux of the star. However, the second requirement for direct detection is that the angular separation of the planet from its parent star must be larger than the inner working angle of system. At fixed mass, this translates into a maximum distance that a Habitable Zone planet can be detected,

$$d_{max} = 10 \text{ pc} \left(\frac{\theta_{IWA}}{100 \text{ mas}} \right)^{-1} \left(\frac{M_*}{M_\odot} \right)^2 \quad (\text{Habitable}). \quad (70)$$

The number of available targets is $\propto n(M_*) d_{max}^3$, where $n(M_*)$ is the volume density of stars of a given mass, i.e., the mass function. Since the exponent of the mass function

in the local solar neighborhood is generally $\gtrsim -2$, this requirement strongly favors high-mass stars. The optimal mass will depend on the precise details of the survey and the nature of the noise sources (see, e.g., Agol 2007), but these arguments demonstrate that we can generically expect the sensitivity of imaging surveys for habitable planets to be fairly strongly peaked at intermediate masses.

- **Transits.** The signal-to-noise ratio, transit probability, and period of a transiting habitable planet scale as,

$$(S/N)_{tr} \propto R_p^2 M_*^{-5/2}, \quad P_{tr} \propto M_*^{-1}, \quad P \propto M_*^{5/2}, \quad (\text{Habitable}) \quad (71)$$

all of which favor or strongly favor low-mass stars. Furthermore, as discussed above, the radial velocity signals of Habitable Zone planets around low-mass stars are also larger and within reach. Finally, low-mass stars are more common. These various considerations have led to the suggestion that transit surveys of low-mass stars may be the most promising route to detecting habitable Earthlike planets (Gould et al. 2003b; Nutzman & Charbonneau 2008; Blake et al. 2008). Indeed, several such surveys are underway or are being planned (e.g., Charbonneau et al. 2009), with the ultimate goal of finding a Earthlike system whose atmosphere can be characterized with, e.g. the James Webb Space Telescope (Deming et al. 2009).

- **Microlensing.** The system parameters which determine the detectability of a given planetary system with gravitational microlensing are the mass ratio q and projected separation s in units of r_E . For a habitable Earthlike planet these are,

$$q \sim 5 \times 10^{-5} \left(\frac{M_p}{M_\oplus} \right) \left(\frac{M_*}{0.5 M_\odot} \right), \quad (72)$$

$$s_{\text{HZ}} \equiv \frac{a_{\text{HZ},\perp}}{r_E} \sim 0.1 \left(\frac{M}{0.5 M_\odot} \right)^{3/2} \left(\frac{d_s}{8 \text{ kpc}} \right)^{-1/2} \left[\frac{x(1-x)}{0.25} \right]^{-1/2}, \quad (\text{Habitable}) \quad (73)$$

where in the expression for s_{HZ} we have assumed a median projection factor such that $a_{\text{HZ},\perp} = 0.866 a_{\text{HZ}}$. Therefore, for typical microlensing host stars, the Habitable Zone distance is much smaller than the Einstein ring. While mass ratios of $q \sim 10^{-5}$ are readily detectable for planets with separations near the Einstein ring ($s \sim 1$), they are much more difficult to detect for planets with $s \ll 1$. This is because these such planets can only be detected when they perturb the inner image created by the primary host star, and then only when this image is close to the primary and thus highly demagnified. See Figure 4. These perturbations are therefore generally quite small. Furthermore, perturbations of the inner image are more strongly suppressed for large source stars (Gould & Gauchere 1997; Bennett & Rhie 1996).

From Equation 73, we see that microlensing favors the detection of habitable planets around higher-mass stars (Di Stefano & Night 2008), and stars that are close to the source or close to the Earth (i.e., such that $x(1-x)$ is small). While current and next-generation ground-based microlensing surveys have essentially no sensitivity to habitable Earthlike planets, specialized surveys for nearby microlensing events, or space-based surveys which boast much larger event rates and detection efficiencies, could potentially detect such systems (Di Stefano & Night 2008; Park et al. 2006; Bennett et al. 2010b; Green et al. 2011).

4 Early Milestones in the Detection of Exoplanets

4.1 Van de Kamp and Barnard’s Star

The pre-1995 literature is scattered with several (presumably) spurious claims of detections of planets around nearby stars. Perhaps the best known early claim is that of van de Kamp, who conducted an astrometric campaign to detect “dark” companions to nearby stars (van de Kamp 1986). Van de Kamp’s lower limits were impressive, typically ruling out Jupiter-mass objects in periods of years to a couple decades, and he reported several stars as having barely-detectable companions of apparently substellar mass. Most intriguing was his report of first one, then later two Jupiter-mass companions to Barnard’s star (GJ 699), the second closest stellar system to Earth.

Van de Kamp made astrometric measurements from the positions of the apparent centroids of stellar images on photographic plates, and targets such as Barnard’s star suffered from having a constantly changing set of astrometric references over his multi-decade survey due to its record-high proper motion (over $10''/\text{yr}$). Subsequent astrometric and radial velocity work have ruled out his claims (Choi et al. 2012, ApJ, submitted, and references therein).

4.2 PSR 1257+12 and the Pulsar Planets

Pulsars are exquisite clocks, typically producing pulses with periods of order $\sim 1\text{--}10^{-3}$ s. Once these periods are corrected for well-measured linear drifts with time and occasional “glitches” (sudden shifts in period), their precision can rival and even surpasses the best atomic clocks on Earth. Successful analysis of pulse arrival times requires carefully solving for the distance and space motion of the pulsar and the removal of the effects of the motion of the observatory.

In 1991, two teams announced having contemporaneously observed unexplained residuals to their timing models indicative of the first known exoplanets: very small, terrestrial-planet-mass companions orbiting their pulsars. Matthew Bailes and Andrew Lyne (Bailes et al. 1991) reported a timing variation with a period of 6 months apparently due to a $10 M_{\oplus}$ companion orbiting the pulsar PSR 1829-10. Meanwhile, Cornell astronomer Alexander Wolszczan had observed a similar sort of signal from a millisecond pulsar, PSR 1257+12, and had recruited Dale Frail of the National Radio Astronomical Observatory to help confirm its position on the sky to perfect the position model. By November 1991 Wolszczan & Frail (1992) had submitted a manuscript on their discovery, and both teams planned to describe their work at the January 1992 meeting of the American Astronomical Society.

At the meeting, Lyne announced that just days earlier he had discovered an error in his timing model. A tiny positional error combined with an insufficiently precise description of the Earth’s orbit had led to the small, periodic, 6-month signal in their residuals that they had mistaken for a planet. With the correct timing model, there was no evidence of a planetary perturber on the pulsar. Lyne’s public and frank admission was acknowledged as a laudable demonstration of scientific integrity by a standing ovation at the meeting and an editorial in *Nature* (Lyne & Bailes 1992; *Nature* 1992; Wolszczan 2012).

The world would not be long with its first exoplanets, however. The very next speaker at the AAS meeting was Wolszczan, whose timing model had correctly accounted for all

important effects. Wolszczan described the first planets known outside the solar system: a pair of bodies with $\sim 4 M_{\oplus}$ orbiting the millisecond pulsar PSR 1257+12 with periods of 66 and 98 days. This system would continue to impress, revealing a third low mass planet to Wolszczan’s team, as well (Wolszczan et al. 2000).

These planets’ formation mechanism is still not understood, and to date no similar system of low mass planets is known. Signals of higher-mass planets orbiting pulsars would continue to be found, however: in particular, Bailes would go on to discover an apparently high-density $1.4 M_{\text{Jup}}$ object orbiting pulsar PSR J1719-1438 (Bailes et al. 2011).

4.3 Early Radial Velocity Work

4.3.1 Campbell & Walker’s survey and γ Cep Ab

In the 1981, Bruce Campbell of the University of Victoria, Gordon Walker of the University of British Columbia, and their team began an ambitious survey for substellar objects orbiting 20 of the brightest nearby stars. They sought to exploit the recently available technologies of high resolution ($R > 40,000$) echelle spectrographs and digital detectors in the form of Reticons and CCDs to achieve the best possible Doppler precision.

To establish an accurate and robust wavelength solution they employed an absorption cell of hydrogen fluoride (HF) which imposed a “picket fence” of regular, strong, narrow, and widely spaced ($\sim 15\text{\AA}$) absorption lines from the $3 \rightarrow 0R$ branch transitions near 8700\AA , far from any telluric features (Campbell et al. 1988). Campbell & Walker had sought a chemical cell that would provide such lines in the optical that would not contaminate the stellar lines, and with few extraneous absorption features from isotopic impurities or other effects. Campbell & Walker found no other chemicals that fit their needs, and so used HF despite the serious difficulties of working with that chemical⁴. To achieve the necessary optical depth and wavelength stability of HF lines, Campbell & Walker stabilized the temperature and pressure of their 1 m long cell at 373 K and connected it to a vessel containing liquid HF in an ice bath, yielding a pressure of roughly 0.5 atm.

The well-known and well-spaced HF lines granted Campbell & Walker unprecedented optical Doppler precision, independent of mechanical and thermal changes in the optics of their spectrograph. This method was, at the time, greatly superior to emission line calibration because the reference lines were measured simultaneously to the stellar exposure and through the same optical path as the stellar photons. Campbell & Walker achieved 10–15 m/s radial velocity precision on most of their sample of 20 stars. This precision is, in retrospect, more than sufficient to detect close-in giant exoplanets, but their sample of stars was simply too small and close-in planets are too rare for them to have discovered a strong exoplanetary signal with any significant likelihood.

Campbell et al. (1988) were able to confirm that objects with $m \sin i = 10\text{--}80 M_{\text{Jup}}$ are rare, and noted several interesting signals near the limits of their detectability. They noted an especially intriguing apparent signal for γ Cep A with a 25 m/s amplitude and 2.7 yr

⁴Campbell & Walker understatedly reported the “obnoxious” nature of HF and that “standard safety precautions of chemical laboratories are appropriate” for this rather dangerous chemical which reacts with glass, forms hydrofluoric acid on contact with water, can painlessly penetrate human tissues, and causes burns that can necessitate amputation (OSHA Occupational Safety and Health Guidelines for HF, US Department of Labor, 2012).

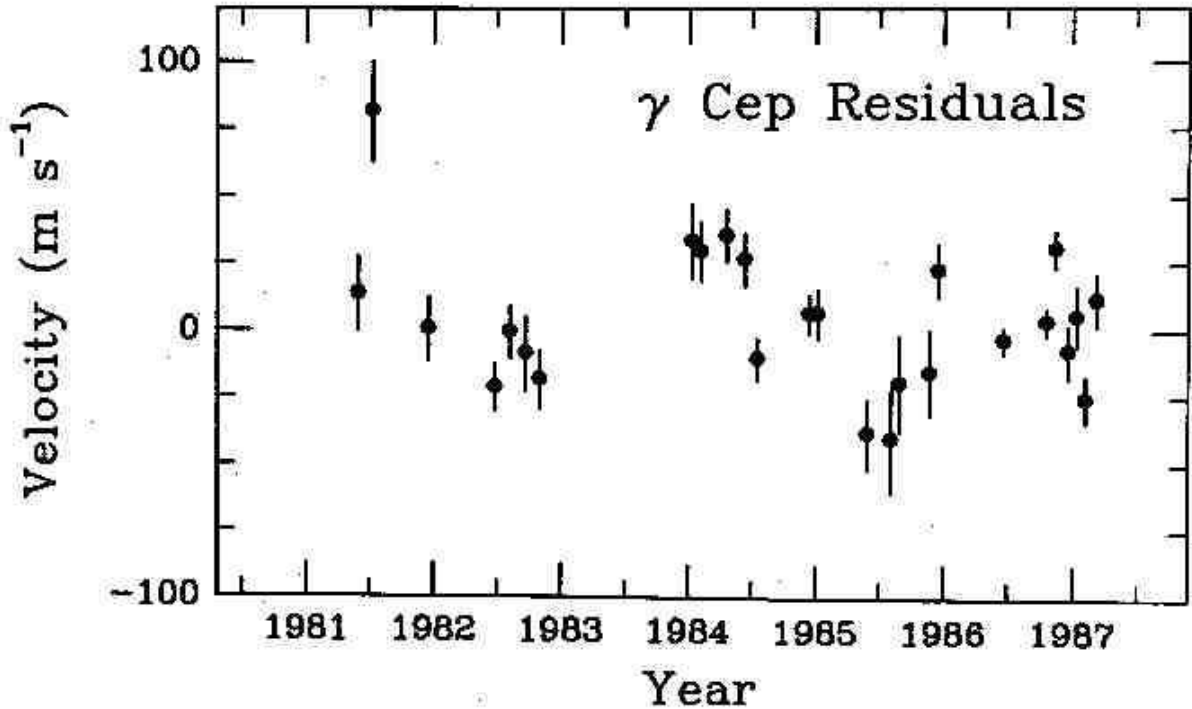


Figure 7: Figure from Campbell et al. (1988) illustrating the first tentative detection of a real exoplanet from the pioneering radial velocity survey. Reproduced by permission of the AAS.

period, superimposed on a long-term acceleration from the star’s binary companion. The implication of this periodicity was that γ Cep A was orbited by a $\sim 1.7 M_{\text{Jup}}$ mass planet at a few AU.

Four years later, Walker et al. (1992) reported on their monitoring of the Ca II 8662Å line and determined that γ Cep had a weak 2.52 yr activity period, uncomfortably close to the purported planetary signal, and cautiously noted that the RV signal was likely due to stellar activity.

Eleven years later, after nearly 100 bona fide exoplanets had been discovered by teams around the world, Hatzes et al. (2003) announced RV monitoring at McDonald Observatory had confirmed Campbell, Walker, & Young’s original detection: the variations were indeed due to a $m \sin i = 1.7 M_{\text{Jup}}$, $P = 2.5$ yr planet, and there was no longer any evidence of a 2.5 yr activity period. In retrospect, Campbell & Walker’s planet search had been a sort of success, after all. It had also inspired subsequent teams to continue their efforts.

4.3.2 Latham’s survey and HD 114762 *b*

In 1988, David Latham of the Harvard-Smithsonian Center for Astrophysics and his team described a new result from their precise radial velocity instrument, the CfA Digital Speedometer at Oak Ridge Observatory. In 1984, Latham and Israeli astronomer Tsevi Mazeh had conducted a short survey of about three dozen early M dwarfs for short period, massive planets using this instrument, but had found nothing (Latham 2012). For this new survey,

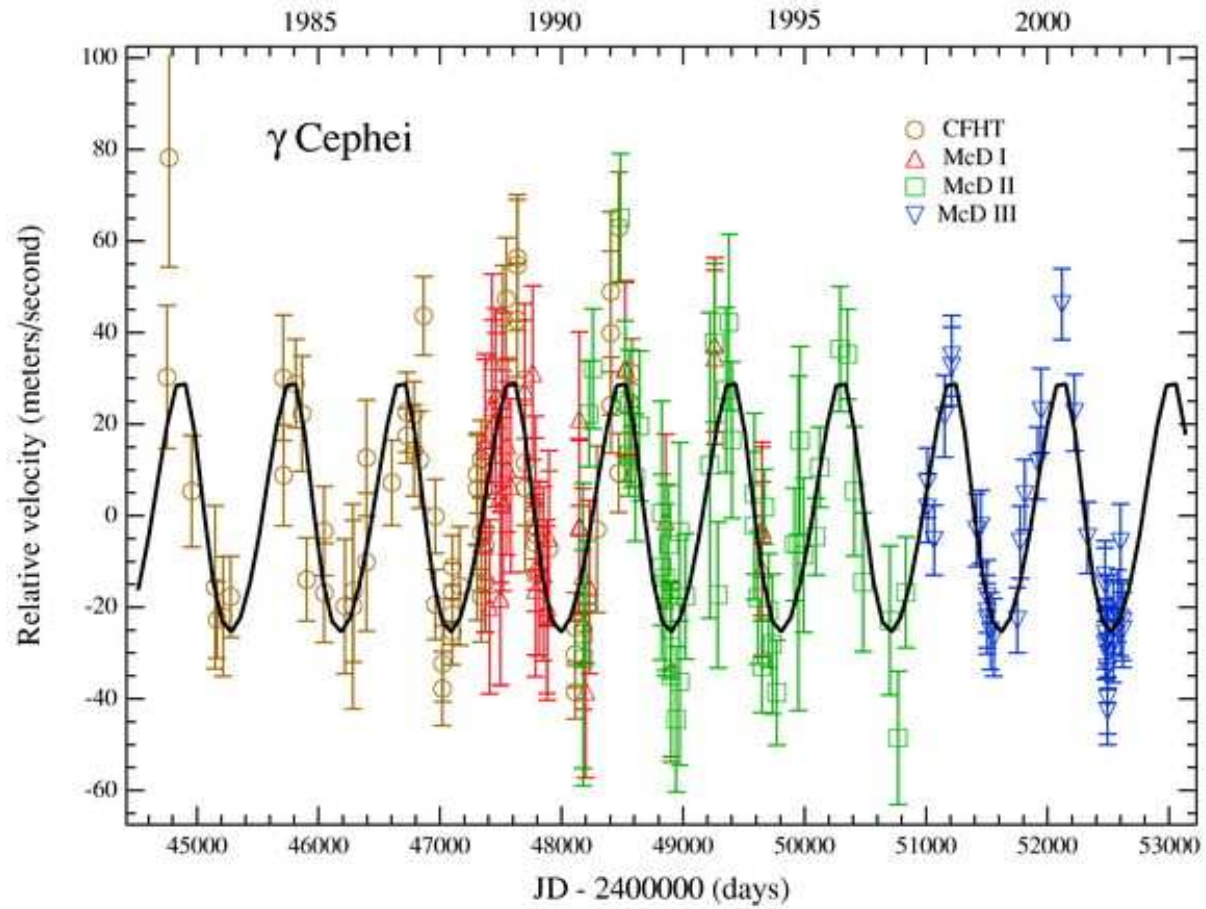


Figure 8: Fig. 3 of Hatzes et al. (2003) showing confirmation data for the planet γ Cep *b*, including the original Campbell et al. data. Reproduced by permission of the AAS.

Latham et al. sought to further stabilize their spectrograph to achieve ~ 100 m/s precision to measure accurate binary orbits and improve the IAU system of radial velocity standards. Latham et al. achieved this stabilization by removing the Cassegrain instrument from the telescope, stabilizing its temperature, and feeding it with a $100\text{-}\mu$ optical fiber. This provided a constant gravity vector, thermal and mechanical stability, and a (relatively) uniformly illuminated entrance slit, robust against guiding errors.

On its first night of operation, Latham et al. (1989) observed several RV standard stars including HD 114762. They noted a large (390 m/s) radial velocity discrepancy from the known value. Curious, they compared their previous measurements made at lower precision and found a highly significant signal at near 84 d with 530 m/s semiamplitude, corresponding to a $13 M_{\text{Jup}}$ companion.

Subsequent observations at high precision confirmed the reality of the signal (see Fig. 9). Latham et al. (1989) had discovered, serendipitously, on the first night of observation, and in a sample of only seven objects, what today would be considered by many to be an exoplanet. At the time, no objects with a mass anything like $13 M_{\text{Jup}}$ were known, and Latham et al. cautiously referred to their object as “a probable brown dwarf”, however they noted that the companion “might even be a giant planet”⁵, a point that was picked up by the media but criticized by many of their colleagues (Latham 2012). Regardless of its taxonomic class, it was the first firm detection of a substellar object beyond the Solar System, and today is often included in catalogs of exoplanets (e.g. Wright et al. 2011).

4.3.3 Marcy & Butler’s iodine survey

In 1992, Geoffrey Marcy and Paul Butler of San Francisco State University announced their survey of 70 nearby stars using an iodine (I_2) cell for wavelength calibration. Previous Doppler work by Marcy & Benitz (1989) had used ThAr emission lamps to search for brown dwarfs orbiting nearby M dwarfs with radial velocity precision of ~ 250 m/s; Marcy & Butler sought to improve this precision by 1–2 orders of magnitude with their iodine cell and the CCD at the high-resolution Hamilton spectrograph, designed by Vogt (1987).

Unlike Campbell & Walker, Marcy & Butler sought an absorption cell that would provide absorption features *throughout* a broad region of wavelength space. Following Libbrecht (1988) (who had employed an iodine cell to study solar sunspots and had extended their studies to p-mode measurements of stars) Marcy & Butler settled on iodine as the ideal absorption gas. Their rationale was that this provided the wavelength reference at every point in the spectrum, not just every 15\AA , and that the potentially problematic blending of stellar features with iodine features could be modeled given a sufficiently accurate template spectrum of the star and the iodine cell (the latter obtained with a Fourier Transform Spectrograph).

Marcy & Butler further sought to model the variable instrumental profile of the spectrograph as a function of wavelength to account for the not insubstantial thermal and mechanical variations in the spectrograph, and for the non-uniform illumination of the entrance slit. Marcy & Butler’s sealed cell was ~ 10 cm long, held at a constant 323 K, and 0.01 atm,

⁵Later, the IAU would provisionally set the deuterium-burning limit for star-like objects, $13 M_{\text{Jup}}$ as the border between planets and brown dwarfs found in orbit around stars. This is useful for purposes of nomenclature, but bears little on issues of formation and composition, and today the distinction is not always honored.

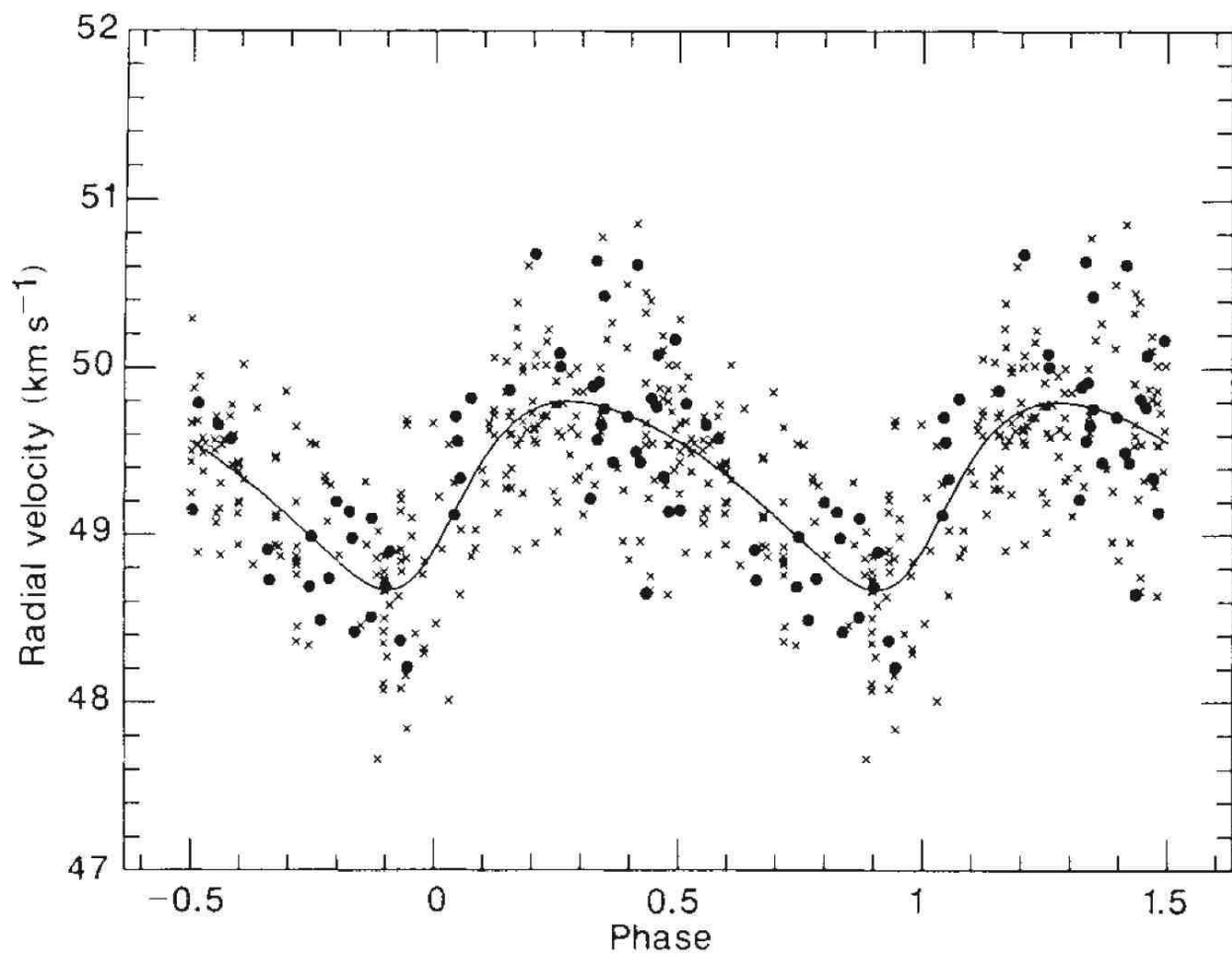


Figure 9: Figure 2 of Latham et al. (1989) illustrating the first firm detection of a substellar object outside the Solar System. In retrospect, the object appears to occupy the high-mass tail of the distribution exoplanets. Figure includes both CORAVEL (filled circles) and CFA Digital Speedometer (crosses) measurements.

and had the further advantage that it was relatively easy to construct and its contents were benign (indeed, medicinal!). Marcy & Butler (1992) reported that they had achieved 25 m/s precision at the beginning of their survey, and foresaw significant improvement through more sophisticated instrumental profile modeling. Indeed, by 1996 Marcy & Butler would demonstrate 3 m/s precision (Butler et al. 1996) and they and their collaborators would go on to be responsible for over half of the exoplanets discovered over the next 15 years.

4.3.4 Hatzes & Cochran’s survey and β Gem *b*

Hatzes & Cochran (1993) reported their results from precise Doppler monitoring of three bright K giants as part of a broader planet detection effort. Their primary technique was to use telluric (atmospheric) O₂ bands as an absorption wavelength reference, which had been reported by Griffin (1973) to be sufficiently stable to allow 10 m/s precision. They found that typical long-term stabilities were more like 20 m/s. They had also begun employing an iodine cell (Cochran & Hatzes 1993), and at this point had obtained a small number of iodine observations.

Hatzes & Cochran found that all three K giants in their sample, Arcturus (α Boo), Aldebaran (α Tau), and Pollux (β Gem) displayed large, periodic radial velocity variations with semiamplitudes of 50-200 m/s. Comparison with prior radial velocities obtained by Campbell’s group (Walker et al. 1989) revealed that the variations were coherent over 10 years. While both α Boo and α Tau showed significant day-to-day RV variations indicative of radial pulsation modes and correlated variations in the 10830Å He I line, β Gem seemed to have a clean signal, consistent with a 554 d planet with a minimum mass of 3 M_{Jup}.

Observations by the Canadian team (Larson et al. 1993) showed that the Ca II 8662Å line showed periodic variation at the same frequency as the RV variations (which they had measured independently). This coincidence cast strong doubt on the planetary interpretation of the β Gem RV variations, especially in light of the much larger and more clearly activity-related variations in α Boo and α Tau.

Hatzes et al. (2006) combined literature data with subsequent iodine observations from McDonald Observatory and Tautenburg Observatory to show that the RV variations continued coherently into 2006 and that the Ca II H & K lines showed no coincident variation. They concluded that the variations in β Gem were likely due to a minimum mass 3 M_{Jup} companion with period 590 d.

4.3.5 Mayor & Queloz and 51 Pegasi *b*

The first unambiguous detection of a planet-mass object orbiting a normal star was by Mayor & Queloz (1995) of Geneva Observatory. Michel Mayor and Didier Queloz used the ELODIE spectrograph, which achieved 13 m/s precision through outstanding mechanical stability. ELODIE (the successor to CORAVEL) was a fiber fed spectrograph within a stable, temperature controlled environment (Queloz et al. 1998). Wavelength calibration was achieved through use of a simultaneous observation of a thorium-argon (ThAr) emission lamp. Mayor & Queloz used cross-correlation with a binary mask to determine the velocity of the stellar spectrum with respect to the known wavelengths in the emission line spectrum. The mechanical stability of the instrument ensured that the offset between the stellar and comparison lamp spectra was fixed and stable, and the scrambling inherent to the fiber

ensured that the position of the stellar spectrum did not suffer significantly from variations in illumination or guiding on the fiber tip.

51 Peg *b* has a semiamplitude of only 59 m/s and period of only 4.2 d, implying a minimum mass of $0.5 M_{\text{Jup}}$. This was a shocking development — planet formation theory had not predicted the existence of such close-in planets⁶, and indeed the tiny mass implied by the detection was smaller than any known binary companion by more than an order of magnitude.⁷ Immediately Marcy & Butler (1995) confirmed the detection, as did Hatzes et al. (1997) soon thereafter. Debate ensued about the nature of the variations and whether they could be due to non-radial pulsation modes (Gray 1997), but the detection of planetary transits would put these concerns to rest: the field of exoplanetary science had begun in earnest. The Geneva team would expand and find great success over the next decades, eventually pushing their precision below 1 m/s with the HARPS spectrograph.

4.4 The First Planetary Transit: HD 209458*b*

The presence of close-in planets provided an opportunity to detect exoplanets directly through transits. The probability that a planet will transit its hosts star is inversely proportional to its orbital distance, and since 51 Peg *b* and similar “Hot Jupiters” orbited at ~ 10 stellar radii from their host stars, their transit probability was around 10%. Photometrists began to monitor these planets’ hosts stars for such events, expecting to find one once the number of known systems approached 10. Concerns over nonradial pulsations also contributed to the desire to monitor stars for photometric evidence of such effects.

Two teams detected the $m \sin i = 0.7 M_{\text{Jup}}$, $P = 3.5$ d planet orbiting HD 209458 independently (Mazeh et al. 2000; Henry et al. 2000) and collaborated with photometrists to conduct the now-standard photometric follow-up prior to publication. Two teams succeeded contemporaneously: their announcements of the detection of the transits of HD 209458 appeared in the literature simultaneously, having been submitted to the *Astrophysical Journal* within one day of each other (Henry et al. 2000; Charbonneau et al. 2000) exemplifying the intense competition to produce exoplanetary “firsts”. This measurement of the orbital inclination and radius (and thus the true mass and density) of the planet dispelled any remaining doubt as to the origins of most of the similar RV variations of stars, and provided the necessary impetus for large-scale efforts to detect more planets with radial velocities, transits, and, soon, microlensing and direct imaging.

4.5 Microlensing

4.5.1 Microlensing History

While the idea of gravitational microlensing by individual stars was considered sporadically over the past century (Einstein 1936; Eddington 1920; Chwolson 1924; Lodge 1919; Liebes 1964; Refsdal 1964), it was the seminal paper by Paczyński (1986) that gave birth to the modern microlensing field. In this paper, Paczyński argued that it would be feasible to

⁶But see the remarkably prescient article by Struve (1952), which all but foresaw this detection, how it would be made, and the subsequent detection of planetary transits.

⁷The third firm detection of a substellar object, the imaging of brown dwarf GJ 299 B, was announced at the same conference as 51 Peg *b*!

monitor several million stars toward the Magellanic clouds on timescales of a few hours to a few years, in order to search for gravitational microlensing events due to foreground massive compact objects that could make up a substantial fraction of the mass of the dark matter halo of the Milky Way. Within a few years, several collaborations were initiated to survey regions in the Large Magellanic Clouds and Galactic bulge to search for microlensing events (Alcock et al. 1993; Aubourg et al. 1993; Udalski et al. 1993). The first detections followed shortly thereafter, and to date of order 10^4 microlensing events have been detected, with the majority seen along the line of sight to the bulge.

Although the original motivation for microlensing surveys was the search for dark matter, it was soon realized that it would be possible to search for planetary companions to the stars and remnants that provided a guaranteed signal for these experiments. Mao & Paczynski (1991) first pointed out that binary lenses whose components were separated by roughly their Einstein ring radius would give to sharp, distinctive light curves features associated with the presence of caustic curves in such systems. Caustics are the set of source positions where extra image pairs are created or destroyed with the source crosses the caustic, resulting in large changes in the total magnification. They also noted that the probability of a source crossing these caustics for a binary lens remained substantial down to mass ratios of $q \sim 10^{-3}$, therefore suggesting that planetary companions could also be detected in this way. Gould & Loeb (1992) consider this idea in detail, refining the estimates for the detection probabilities for different planet mass ratios, and discussing the practical requirements for carrying out an exoplanet survey with microlensing. In particular, they advocated a two-tier strategy, whereby survey collaborations use a single dedicated telescope equipped with a wide-field camera monitor large areas of the sky to identify and alert stellar microlensing events before peak, and follow-up collaborations with access to several longitudinally-distributed, narrow-angle telescopes follow particularly promising events at much higher cadence to search for the brief planetary deviations. The first microlensing planet surveys began in 1995, with the first real-time alerts from the survey collaborations (e.g., Udalski et al. 1994; Alcock et al. 1996), and subsequent monitoring of these alerts by several follow-up collaborations (Alcock et al. 1996; Albrow et al. 1998; Rhie et al. 2000).

Ongoing surveys over the next 6 years (1995-2001) failed to detect any planetary microlensing events. The primary reason for this is that the total number of events alerted by the survey collaborations was relatively low ($\lesssim 100$), and therefore there were typically few events ongoing at any given time that were both suitable for follow-up and very sensitive to planets. In particular, there were only a handful of high-magnification events per year, which had been recognized to be intrinsically very sensitive to planetary companions (Griest & Safizadeh 1998). Nevertheless, this phase was important for the field, as the real-world struggles involved with carrying out and analyzing the results from these surveys, including the ensemble of non-detections (Gaudi et al. 2002; Snodgrass et al. 2004), naturally led to the development and maturation of both the theory and practice of the method.

4.5.2 First Planet Detections with Microlensing

The first detections of planets with microlensing were enabled primarily by a series of upgrades by several survey collaborations to their observational setups. In 2001, the OGLE collaboration initiated their third phase with an upgrade to a new camera with a 16 times larger field of view. With this larger field of view, they were able to monitor a larger area

of the Galactic bulge with higher cadence, and as a result began alerting ~ 500 microlensing events per year. This higher event rate, combined with improved cooperation between the survey collaborations, led to the first planet discovery in 2003 by the Microlensing Observations in Astrophysics (MOA) and OGLE collaborations (Bond et al. 2004). Shortly thereafter, the MOA collaboration upgraded to a 1.8m telescope with a 2 deg² camera (Sako et al. 2008). By 2007, the MOA and OGLE collaborations were sending alerts for nearly 1000 microlensing events per year, thus enabling a substantial increase in the rate of planet detections.

The light curve data and best-fit model for the first microlensing planet discovery are shown in Figure 10. This is a “cold Jupiter”: the planet has a mass $M_p \sim 3 M_{\text{Jup}}$ and orbits a star with $M_* \simeq 0.6 M_\odot$ at a separation of $a \sim 4\text{AU}$, or ~ 2.5 times the snow line distance (Bennett et al. 2006).

To date, 14 microlensing planet detections have been published. The masses and semi-major axes of these planets are shown in Figure 5, they span nearly three decades in mass from a few times the mass of the Earth to several times the mass of Jupiter, and are spread over a factor of ~ 5 in separation, centered at a few times the snow line distance. Notable among these detections are the first discovery of a “cold SuperEarth” (Beaulieu et al. 2006), and the first discovery Jupiter/Saturn analog (Gaudi et al. 2008; Bennett et al. 2010a).

5 State of the Art

5.1 Astrometry

Astrometric precision has improved considerably since van de Kamp’s work, and the first verifiable astrometric discovery of an exoplanet appears imminent. Pravdo & Shaklan (2009) announced that their long-term astrometric monitoring of the ultra-cool dwarf star vB 10 had revealed a $\sim 6M_{\text{Jup}}$ companion in a 9 month orbit, however subsequent followup with radial velocities determined that the signal was spurious (Bean et al. 2010; Anglada-Escudé et al. 2010; Lazorenko et al. 2011).

More promisingly, Muterspaugh et al. (2010) used an optical interferometer to carefully measure the astrometric motions of binary stars, and combined these measurements with radial velocities of the systems to search for low mass companions to stars in tight binaries. The project concluded with six planetary candidates, including two “high confidence” members that could prove to be the first astrometrically detected exoplanets. If real, these planets will put strong constraints on planet formation theories in binary systems.

The astrometric detection of planets discovered by other means has produced substantially more results, primarily because the approximate astrometric signals are known from prior radial velocity work and so searches are more efficient. Most fruitful has been work on nearby stars employing the *Hubble Space Telescope* Fine Guidance Sensor, which is capable of precise astrometry of bright stars. This has revealed some high-mass planet candidates from radial velocity surveys to be binary stars in face-on orbits, and has revealed the mutual inclinations of planets in multiplanet systems (Bean et al. 2007; Bean & Seifahrt 2009; McArthur et al. 2010).

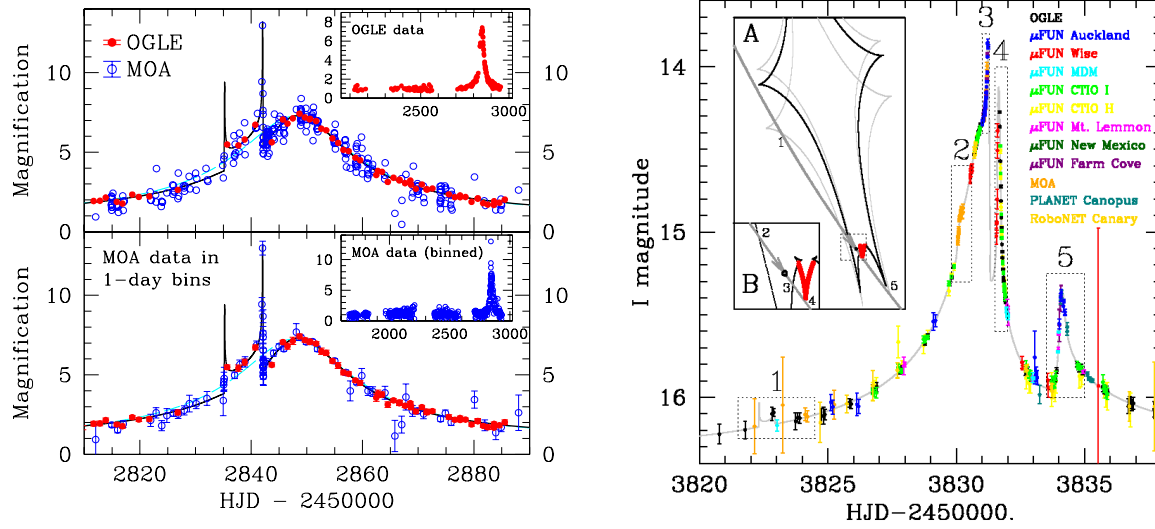


Figure 10: (Left) The first discovery of an exoplanet with microlensing in the OGLE 2003-BLG-235/MOA 2003-BLG-53 event (Bond et al. 2004). The red and blue points show the data from the OGLE and MOA collaborations, respectively. The top large panel shows the native data, whereas the MOA data have been binned into 1 day bins in the bottom panel. The black and cyan curves show the best fit planetary and single lens model, respectively. The planetary companion is revealed through the brief deviation from the smooth symmetric curve arising from the host star, including the well-covered sharp spike near HJD-2450000~2842 caused by the source crossing a caustic created by the planetary companion. The small insets show the full, multi-year data spans for the OGLE and MOA data. From Bond et al. (2004), reproduced by permission of the AAS. (Right) The OGLE-2005-BLG-109 microlensing event, arising from a star with a Jupiter/Saturn analog two-planet system. Panel A shows the source trajectory through the caustic created by the two planets (dark gray curve). The five light curve features are caused by the source crossing or approaching the caustic, and the locations of these features indicated with numbers. The majority of the caustic (in black) is due the Saturn-analog planet, which explains 4 of the 5 features. The portion of the caustic arising from the Jupiter-analog planet is shown in red. This additional caustic is required to explain the fourth feature in the light curve. The light gray curves show the caustic at the time of features 1 and 5. Panel B shows the detail of the source trajectory and caustic near the times of the second, third, and fourth features. From Gaudi et al. (2008).

5.2 Imaging

5.2.1 2M1207b

Chauvin et al. (2010) describe their survey of young, nearby stars for low mass, possibly planetary companions using the ESO/VLT 8-m telescope equipped with the NACO AO system and infrared camera. They began their survey in 2002 during commissioning, and targeted, among other things, the lowest mass members of known, nearby, young stellar associations. This allowed them to maximize the separation and contrast of companions and push coronagraphy into the planetary-mass regime.

After some promising detections of higher mass objects, the survey bore fruit when Chauvin et al. (2004) detected a very low mass companion to the M8 TW Hydra association (TWA) brown dwarf 2MASSW J1207334-393254 (called 2M1207; Figure 11) at a separation of only $0''.8$ (~ 55 AU). Membership in the TWA yielded an age for the companion, and a distance was estimated from the colors and brightness of 2M1207. Comparison with models of the thermal evolution of young objects (Burrows et al. 1997; Chabrier et al. 2000; Baraffe et al. 2002) allowed Chauvin et al. (2004) to estimate the companions mass to be $\sim 5 M_{\text{Jup}}$, assuming that it was indeed a bound, coeval object and not a background contaminant.

Chauvin et al. (2005) followed up their prior observations to confirm common proper motion using the same instrument. They demonstrated that the two objects share proper motion and parallactic motion with this star, all but proving that they form a bound pair.

The nature of 2M1270b was, and still is, unclear. Its status as a “planetary-mass” object seems secure, but its wide separation (55 AU) and ~ 0.2 mass ratio with its primary made the pair perhaps more analogous to a scaled-down binary star system than a planet-star system. Chauvin et al. (2005) noted that a protoplanetary disk origin for the *b* component seemed unlikely. Nonetheless, they had acquired the first image of a planet, by mass if not by formation mechanism, and this presaged the many more successes to come from high contrast imaging. The ESO/VLT group would go on to detect the planet-mass object AB Pic *b* and many faint stellar companions to nearby stars, including many planet hosts (Chauvin et al. 2010).

5.2.2 Fomalhaut *b*

Kalas et al. (2005) used the *Hubble Space Telescope* (*HST*) Advanced Camera for Surveys (ACS) to image the dust belt orbiting Fomalhaut (α Piscis Austrini), a ~ 400 Myr-old A4 dwarf at 7.7 pc. Debris disks or belts are a common feature of many young main sequence stars, typically with structure consistent with dynamical interactions from unseen planets (see chapter by Moro-Martin). The coronagraphic mode of ACS allowed the *HST* team to make a spectacular and detailed image of the disk in reflected optical light, revealing that its dominant feature is a highly inclined, off-center belt with an apparently sharp inner edge at 133 AU radius. The 15 AU geometric offset of the belt from the star and the sharp inner edge could be explained by the presence of a planetary companion with non-zero eccentricity “sculpting” the inner edge of the belt and maintaining the geometric offset via secular perturbation (Wyatt et al. 1999).

Follow-up observations to determine the structure of the disk using a variety of PSF subtraction techniques allowed Kalas et al. (2008) to confirm a persistent source with optical

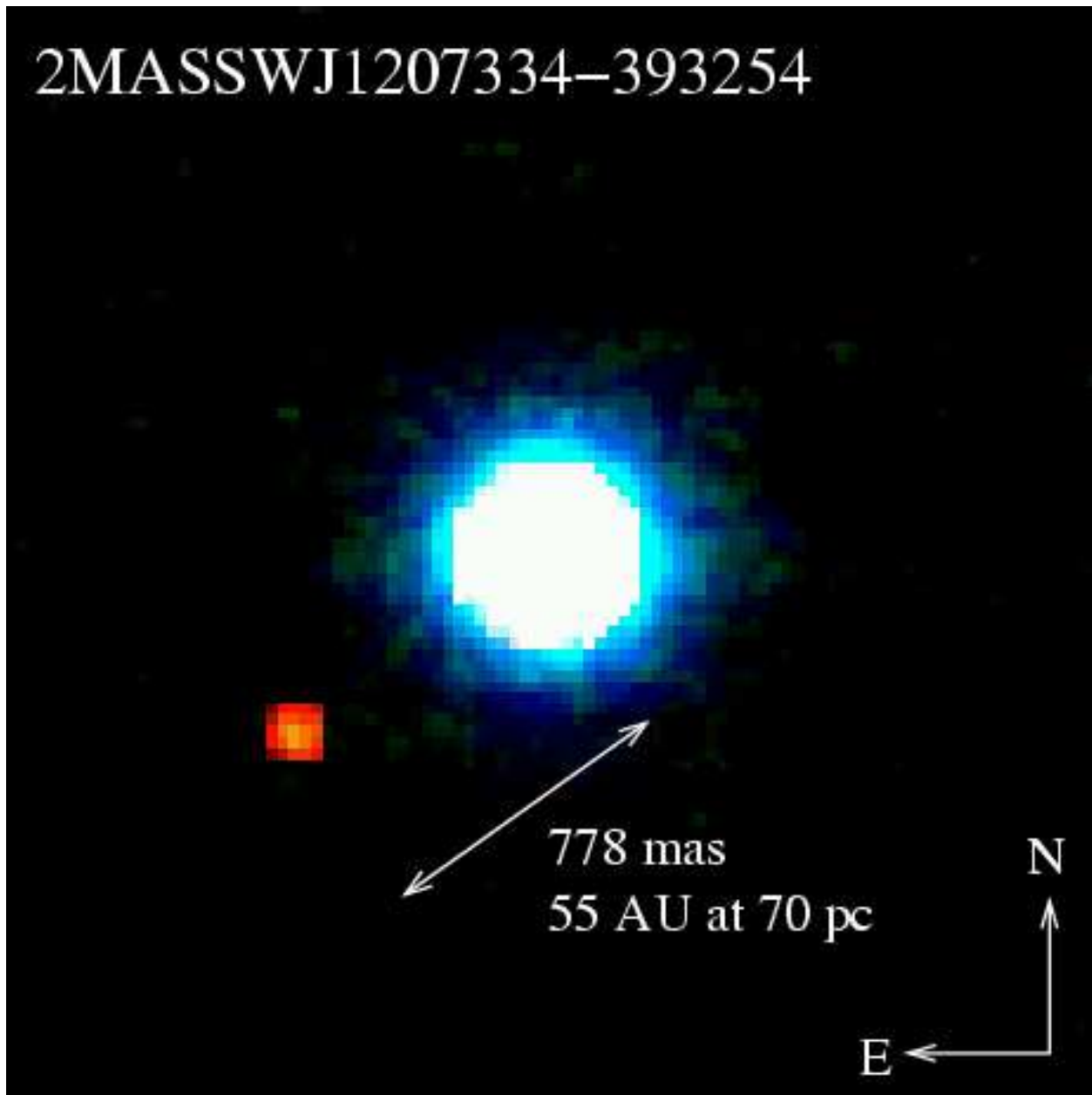


Figure 11: NACO image of 2M1207*b*. The primary is a M8 dwarf at ~ 70 pc; the secondary is much cooler late L dwarf with probable mass $\sim 5M_{\text{Jup}}$. From Chauvin et al. (Fig. 11 2004, credit G. Chauvin & ESO).

brightness ~ 25 mag and located $\sim 13''$ away from the primary star, just inside the belt, and consistent with the “sculpting” hypothesis. Comparison of multiple epochs allowed Kalas’s team to measure the orbital motion of the object astrometrically and confirm that it is a proper motion companion of Fomalhaut.

Puzzlingly, this very faint companion did not appear in their infrared imaging at the Keck 10-m and Gemini 8-m telescopes, which is inconsistent with the optical emission being thermal in origin according to current models. Kalas et al. were able to use the dust disk itself to constrain the object’s mass dynamically to be $< 3M_{\text{Jup}}$ (Chiang et al. 2009), and thus the lowest mass directly imaged planet candidate to date. Kalas et al. (2008) proposed several possible explanations for Fomalhaut b’s unusual optical brightness, such as reflection from a circumplanetary dust ring that could be as large as 35 planetary radii, though still significantly smaller than Saturn’s Phoebe ring. They also proposed an alternative model where reflected light is due to a transient dust cloud produced by a rare destructive collision between two analogs of solar system Kuiper Belt objects.

As with 2M1207b, ascertaining the nature of Fomalhaut *b* will require additional observations and theoretical input. It orbits an intermediate mass star with semi-major axis ~ 120 AU, and is still undetected in the infrared. Whatever its nature, its presence in a disk of material strongly implicates a disk origin for the object, and provides hope for more secure similar detections of similarly bright planetary objects in the future.

5.2.3 Beta Pictoris *b*

β Pic is an A star with a prominent, edge-on debris disk that was the first to be imaged in optical scattered light (Smith & Terrile 1984). One unexpected result was that the disk had several asymmetries in structure (Kalas & Jewitt 1995), including a vertical warp in the disk midplane at < 100 AU projected radius from the star (Burrows et al. 1995). These and other phenomenon observed toward β Pic indirectly suggested the existence of a planetary system, and β Pic *b* was finally directly imaged using VLT/NACO (Lagrange et al. 2009). As with Fomalhaut, the debris disk structure could be used to constrain the planet mass through dynamical theory (Mouillet et al. 1997), as an alternative to mass estimates based on planet luminosity models. Its measured L' brightness of 11th mag corresponds to a $\sim 8 M_{\text{Jup}}$ planet at age ~ 10 Myr.

β Pic *b* is currently unique among the directly imaged exoplanets for having the smallest semi-major axis, which, at ~ 8 AU, corresponds to the approximate ice-line of the system. Unfortunately, the projected separation is also very small, $0''.4$, and follow-up spectroscopic study has yet to be obtained. Systems such as β Pic are therefore ideal targets for the next generation of extreme adaptive optics instrumentation discussed below. These future results will provide important tests of various planet formation and luminosity evolution models, which in the 10 Myr-age regime offer significantly different predictions for the physical properties of Jupiter-mass planets.

5.2.4 The HR 8799 Planetary System

A US/Canadian team led by Marois used AO coronagraphy on the Keck and Gemini telescopes in angular differential imaging mode (ADI, Marois et al. 2006), which exploits the rotation of the field of view on an altitude/azimuth telescope with time to distinguish (and

subtract) PSF features from astrophysical sources. Marois’ team observed the nearby (40 pc) A star HR 8799, which was known to have an IR excess and to be relatively young (20–160 Myr), making any orbiting planets likely to be bright in the near infrared. Marois et al. (2008) reported the discovery of three faint companions to HR 8799, with proper motions consistent with HR 8799 and detectable orbital motion. Comparison with Pleiades brown dwarf brightnesses demonstrated that these objects had likely masses below $11 M_{\text{Jup}}$. Further observations at Keck Observatory allowed Marois et al. (2010) to discover a fourth, *e* component to the system. The projected orbital separations of the four planets range from 14–70 AU.

This family of objects, the first imaged multi-planet system, poses special challenges for planet formation theory. Marois et al. (2010) argue that their masses and orbital radii (and the relative scarcity of other systems such as this) are inconsistent with both in situ gravitational-instability disk fragmentation and core-accretion scenarios. Like the close-in “hot Jupiters”, these distant planets would seem to implicate migration in a disk as a primary architectural factor in planetary system formation.

5.2.5 SPHERE, GPI, and Project 1640

Several “extreme” adaptive optics systems with coronagraphs are in development or operation, and will be capable of detecting young (< 1 Gyr) giant planets at a few diffraction widths from the position of a bright star. Such systems employ deformable mirrors with several hundreds to thousands of actuators, and typically observe bright stars in the near infrared. They use integral field spectrographs produce data cubes (i.e. a low resolution spectrum at each angular position) and can exploit field rotation to employ a variety of PSF subtraction and speckle suppression techniques. They thus produce large data volumes, including spectra of their imaged planets, and will typically have narrow fully-corrected fields of view ($< 1''$).

Project 1640 (Hinkley et al. 2011), already in operation, is a collaboration between the American Museum of Natural History and the University of Cambridge. It employs the PALM 3000 adaptive optics system on the Hale 200-in telescope at Palomar Observatory. SPHERE (Beuzit et al. 2006) and GPI (Macintosh et al. 2008) are next-generation coronagraphic imagers on the VLT and Gemini South telescopes, respectively. Both will employ thousands of actuators and execute campaigns to discover young Jupiter-mass planets orbiting at several AU from the nearest Sun-like stars. Depending on the adopted planet formation and luminosity evolution model, the detection rate predicted for GPI ranges between 10% and 25%, given a target sample with age < 100 Myr within 75 pc (McBride et al. 2011). Therefore, if these instruments observe ~ 500 stars from this sample, then there will be at least 50 new exoplanets discovered and characterized via direct imaging.

5.3 Rocky and Habitable Worlds

5.3.1 HARPS, Keck/HIRES, and the Planet Finding Spectrograph

The first RV-discovered planets had typical Doppler amplitudes of ~ 50 –500 m/s; the 10 m/s barrier was breached several times between 2000–2005, and detections between 2–5 m/s were common between 2005–2010. The primary instruments making these detections were the

HIRES instrument on the Keck I telescope (operated by various teams of Marcy & Butler) with precision as low as 1–3 m/s, and the HARPS spectrograph (with its heritage from the Geneva team) which regularly achieves precision below 1 m/s on bright stars. Several next generation planet finding spectrographs are being built or commissioned at this writing, including the Planet Finding Spectrograph at Magellan, HARPS-North, and ESPRESSO.

There are two primary obstacles to further precision in radial velocity surveys towards the 10 cm/s necessary for the detection of true Earth analogs. The first is an instrumental stability issue: calibrating the wavelength solution of spectrographs to an order of magnitude better precision than previously possible. For emission-lamp calibration, a fundamental limit is the lifetime and stability of the thorium-argon lamps used as wavelength fiducial. A promising solution is the use of laser frequency combs, which provide essentially arbitrary levels of wavelength precision. Such devices will be used in HARPS-North and ESPRESSO. Also of importance is understanding and maximizing the consistency of the illumination of the output fibers used to guide light to the spectrograph.

For absorption-cell instruments, the practical limit is one’s ability to model the system, in particular the absorption cell, the slit illumination function, the instrumental profile, and the star itself. Progress here is primarily made through careful FTS scans of the actual cell used at the telescope, improved modeling techniques that account for scattered light, and better deconvolution techniques for acquiring stellar templates.

The second obstacle is that of the fundamental stability of the stars themselves. Stars experience p-mode oscillations at the few m/s level that must be either modeled or averaged over. Stellar magnetic surface activity also contributes to radial velocity signatures in many ways, most importantly through rotationally modulated spots and plage, and perhaps through long-term stellar cycles. Modeling and mitigating these effects, perhaps through careful use of contemporaneous photometry, will be necessary to achieve the next large improvement in RV precision for the next generation of planet searches.

5.3.2 Space-Based Transit Surveys

Transit surveys for rocky planets around solar-type stars require extremely precise relative photometry. The fractional depth of the transit of an Earth-sized planet passing in front of a solar radius star is only $\delta \sim 8 \times 10^{-5}$. While relative photometry at a few times this level has been achieved from the ground for individual bright stars with specialized techniques (e.g., Johnson et al. 2009; Southworth et al. 2009; Colón et al. 2010), obtaining $\lesssim 10^{-4}$ relative photometry for the large ensembles of stars required to detect numerous transiting systems is probably out of reach for ground-based surveys, due to unavoidable systematics arising from variations due to the Earth’s atmosphere. The stability afforded by space-based surveys, on the other hand, enables relative photometry for large numbers of stars that is limited primarily by photon and astrophysical noise. Furthermore, for space-based surveys it is possible to obtain continuous photometry for very long periods of time, without diurnal or weather interruptions. This eliminates the aliasing problems that are germane to single-site ground-based transit surveys, and enables the detection of long period transiting systems, which, due to the low duty cycles and long transit durations, are extremely difficult to detect from the ground.

CoRoT is a CNES-led space mission with participation from ESA and other international partners, with the primary goals of studying stars via asteroseismology and detecting tran-

siting planets (Baglin 2003). The 27cm telescope was launched in December 2006, and is located in a Low Earth Orbit. CoRoT is equipped with a 3.05° by 2.7° camera that primarily monitors fields in two different areas of the sky, located toward Galactic longitudes of $\sim 40^\circ$ and $\sim 210^\circ$ (Auvergne et al. 2009). There are two dwell times for the fields; long fields are typically observed for ~ 150 days, whereas short fields are observed for ~ 30 days. To date more than 130,000 stars in ~ 20 fields have been monitored with a cadence of 8.5 minutes (Michel & Baglin 2012). The stellar populations of these fields vary dramatically, but anywhere from 40 – 60% of the targets are expected to be dwarf stars suitable for transit surveys (Cabrera et al. 2009; Erikson et al. 2012). Over the typical $R \sim 12 - 16$ magnitude range of the targets, CoRoT achieves relative photometry on time scales of ~ 2 hours at the level of $\sim 10^{-4}$ at the bright end, degrading to $\sim 10^{-3}$ at $R \sim 16$ (Aigrain et al. 2009). The precision and cadence is sufficient to detect Jupiter-sized companions over the entire magnitude range, whereas Neptunes and Super-Earths can be detected around the brighter stars (e.g., Cabrera et al. 2009).

To date, CoRoT has announced over 20 detections of transiting planets and brown dwarfs. Notable among these discoveries are the detection of a transiting brown dwarf with a mass of $\sim 60 M_{\text{Jup}}$ (Bouchy et al. 2011), the detection of a Jupiter-sized planet with a relatively long period of ~ 95 days (Deeg et al. 2010), and the first detection of a transiting Super-Earth, with a radius of $\sim 1.7 R_\oplus$ and a mass of $3 - 10 M_\oplus$ (Léger et al. 2009).

Kepler is a NASA mission launched in March of 2009, with the primary goal of measuring the frequency of rocky planets in the Habitable Zones of sunlike stars (Borucki et al. 2010). To accomplish this, the 0.95m *Kepler* telescope situated in an Earth-trailing orbit is monitoring a 105 square degree field-of-view near the constellation Cygnus continuously over the 7+ year lifetime of the mission. Light curves of $\sim 200,000$ stars have been obtained over the course of the mission, with typical sampling cadences of ~ 30 minutes, amounting to $\sim 24,000$ observations over the first ~ 500 days of the mission for the subset of stars monitored continuously during this time (Batalha et al. 2012). A subset of stars have higher cadences of ~ 1 minute. The majority of the target stars are solar-type dwarfs with $T_{\text{eff}} \sim 5000 - 6500$ K and $\log g \sim 4.5$, but the full range of target properties span $T_{\text{eff}} \simeq 3500 - 10,000$ K and $\log g \simeq 3 - 5$ (Batalha et al. 2012). The photometric precision and intrinsic stellar variability of this sample is discussed in Gilliland et al. (2011). Relevant to the primary mission goal, the photometric variability for $V \lesssim 12$ stars on transit time scales is $\sim 3 \times 10^{-5}$, quite an impressive figure, but $\sim 50\%$ larger than originally anticipated, primarily due to the fact that typical target stars turn out to be a factor of ~ 2 times more variable than the Sun, probably due to their relative youth. Although this increased noise reduces the expected sensitivity and so yield of the mission for habitable Earthlike planets, this reduced sensitivity was offset with a mission extension (Gilliland et al. 2011).

Although the data set is not yet sufficient to reliably detect true Earth analogs, the exquisite photometric precision and large sample size has already enabled an fantastic array of science. In particular, based on the first ~ 500 days of data, a total of $\sim 2,300$ transiting planets candidates have been identified (Batalha et al. 2012), including ~ 360 multi-planet systems (Fabrycky et al. 2012). The majority of these candidates are smaller than Neptune. Despite the fact that a small fraction of these signals have been confirmed by either radial velocity or transiting timing methods, the overwhelming majority of these signals are expected to be due to real planets, from a number of lines of evidence (e.g., Morton & Johnson 2011; Lissauer et al. 2012). Over 30 systems have been confirmed from various methods, including

a system with six transiting planets (Lissauer et al. 2011), the first discovery of a circumbinary planet (Doyle et al. 2011), and several planets with radius of $\lesssim R_{\oplus}$ (Muirhead et al. 2012; Fressin et al. 2012).

The masses and semimajor axes of the confirmed *CoRoT* and *Kepler* systems with mass measurements as of Dec. 2011 are shown in Figure 5. Comparing these to the planets discovered by ground-based transit surveys highlights the large expansion of discovery space that is enabled by going to space.

5.3.3 Second Generation Microlensing Surveys

Microlensing exoplanet searches are currently in the midst of a transition to the second generation of surveys that will enable the routine detection of rocky planets. Although there have been substantial modifications and upgrades to the details of the “two-tier” survey strategy initially suggested by Gould & Loeb (1992), up until very recently this basic approach has been in use. Second generation surveys will operate in a very different manner. With the development of very large format CCD cameras with fields of view of a square degree or greater, it becomes possible to monitor tens of square degrees of the Galactic bulge containing roughly 100 million stars with cadences of tens of minutes. These cadences are sufficient to detect both the primary event *and* detect the perturbations from low-mass ($\sim M_{\oplus}$) planets, therefore obviating the need for a follow-up observations and allowing for more uniform data and a more objective detection criteria. In order to detect all the planetary perturbations, including those that last less than a day, a longitudinally-distributed network of 1 – 2m class telescopes equipped with such wide FOV cameras is required.

The transition to the next generation survey model began in 2006 when MOA upgraded to the dedicated MOA-II telescope in New Zealand, which has a diameter of 1.8m and 2.2 deg² FOV (Sako et al. 2008; Hearnshaw et al. 2006). In 2010, OGLE upgraded to the 1.4 deg² OGLE-IV camera on their dedicated 1.3m telescope in Chile (Udalski 2009). The Wise Observatory 1.0m telescope in Israel recently been equipped with a 1 deg² camera (Gorbikov et al. 2010). These three groups are collaborating to continuously monitor an ~ 8 deg² region of the bulge with cadences of 15-30 minutes (Shvartzvald & Maoz 2012), and the first planet detection with this strategy was recently announced (Yee et al. 2012).

The next milestone in the development of second generation microlensing surveys will be the completion of the Korean Microlensing Telescope Network (KMTNet). KMTNet is an ambitious, fully funded plan by the Korean government to build three identical 1.6m telescopes with 4 deg² FOV cameras. These will be located in South America, South Africa, and Australia. First light for the final telescope is scheduled for late 2014.

These second generation surveys are expected to increase the planet yields by roughly an order of magnitude over current surveys (Bennett 2004; Shvartzvald & Maoz 2012), and enable the detection of Earth-mass planets, as well as free-floating planets with masses greater than $\sim 10 M_{\oplus}$.

6 Conclusions

In the roughly two decades since the first detections of planets outside the solar system, the field of exoplanets has grown enormously, developing into one of the forefront research

areas in astronomy. The count of confirmed planets is now over 700, with the sample doubling in size every few years at the current rate. New techniques, methods, experiments, instruments, telescopes and satellites to detect exoplanets are constantly being developed, and are enabling the detection and characterization of an increasingly broad diversity of planets orbiting a wider and wider range of hosts. These efforts are not only continually uncovering new and unexpected types of planetary systems, but are beginning to allow for the robust statistical characterization of the demographics of large samples of exoplanets spanning a wide range of parameter space. These efforts ultimately serve to allow us achieve the more general goals of placing our solar system in the context of planetary systems through the Galaxy, understanding the physics of planetary formation and evolution, and determining the frequency of habitable and inhabited worlds.

ACKNOWLEDGMENTS

B.S.G. would like to thank Thomas Beatty and Karen Mogren for permission to discuss results in advance of submission, and acknowledges support from NSF CAREER Grant AST-1056524.

J.T.W. acknowledges support by funding from the Center for Exoplanets and Habitable Worlds. The Center for Exoplanets and Habitable Worlds is supported by the Pennsylvania State University, the Eberly College of Science, and the Pennsylvania Space Grant Consortium.

This work makes extensive use of NASA’s Astrophysics Data System, the Exoplanet Orbit Database at exoplanets.org, and the Extrasolar Planets Encyclopedia at exoplanet.eu.

References

- Aigrain, S., Pont, F., Fressin, F., et al. 2009, *A&A*, 506, 425
 Agol, E., Steffen, J., Sari, R., & Clarkson, W. 2005, *MNRAS*, 359, 567
 Agol, E. 2007, *MNRAS*, 374, 1271
 Albrow, M., Beaulieu, J.-P., Birch, P., et al. 1998, *ApJ*, 509, 687
 Alcock, C., Akerlof, C. W., Allsman, R. A., et al. 1993, *Nature*, 365, 621
 Alcock, C., Allsman, R. A., Alves, D., et al. 1996, *ApJ*, 463, L67
 Anglada-Escudé, G., Shkolnik, E. L., Weinberger, A. J., Thompson, I. B., Osip, D. J., & Debes, J. H. 2010, *ApJ*, 711, L24
 Applegate, J. H. 1992, *ApJ*, 385, 621–629
 Aubourg, E., Bareyre, P., Bréhin, S., et al. 1993, *Nature*, 365, 623
 Auvergne, M., Bodin, P., Boissard, L., et al. 2009, *A&A*, 506, 411
 Baglin, A. 2003, *Advances in Space Research*, 31, 345
 Bailes, M., Lyne, A. G., & Shemar, S. L. 1991, *Nature*, 352, 311
 Bailes, M., Bates, S. D., Bhalariao, V., et al. 2011, *Science*, 333, 1717
 Bakos, G., Noyes, R. W., Kovács, G., et al. 2004, *PASP*, 116, 266
 Batalha, N. M., Rowe, J. F., Bryson, S. T., et al. 2012, *arXiv:1202.5852*
 Ballard, S., Fabrycky, D., Fressin, F., et al. 2011, *ApJ*, 743, 200
 Baraffe, I., Chabrier, G., Allard, F., & Hauschildt, P. H. 2002, *A&A*, 382, 563

- Bean, J. L., McArthur, B. E., Benedict, G. F., et al. 2007, *AJ*, 134, 749
- Bean, J. L., & Seifahrt, A. 2009, *A&A*, 496, 249
- Bean, J. L., Seifahrt, A., Hartman, H., Nilsson, H., Reiners, A., Dreizler, S., Henry, T. J., & Wiedemann, G. 2010, *ApJ*, 711, L19
- Bean, J. L., Seifahrt, A., Hartman, H., et al. 2010, *ApJ*, 713, 410
- Beaulieu, J.-P., Bennett, D. P., Fouqué, P., et al. 2006, *Nature*, 439, 437
- Bennett, D. P. 2004, *Extrasolar Planets: Today and Tomorrow*, 321, 59
- Bennett, D. P. 2008, *Exoplanets: Detection, Formation, Properties, Habitability*, ed. J. Mason (Berlin, Springer) 47-88
- Bennett, D. P., & Rhie, S. H. 1996, *ApJ*, 472, 660
- Bennett, D. P., & Rhie, S. H. 2002, *ApJ*, 574, 985
- Bennett, D. P., Anderson, J., Bond, I. A., Udalski, A., & Gould, A. 2006, *ApJ*, 647, L171
- Bennett, D. P., Anderson, J., & Gaudi, B. S. 2007, *ApJ*, 660, 781
- Bennett, D. P., Rhie, S. H., Nikolaev, S., et al. 2010a, *ApJ*, 713, 837
- Bennett, D. P., Anderson, J., Beaulieu, J. P., et al. 2010b, *arXiv:1012.4486*
- Beuzit, J.-L., Feldt, M., Dohlen, K., et al. 2006, *The Messenger*, 125, 29
- Blake, C. H., Bloom, J. S., Latham, D. W., et al. 2008, *PASP*, 120, 860
- Bond, I. A., Udalski, A., Jaroszyński, M., et al. 2004, *ApJ*, 606, L155
- Borucki, W. J., Koch, D., Basri, G., et al. 2010, *Science*, 327, 977
- Bouchy, F., Deleuil, M., Guillot, T., et al. 2011, *A&A*, 525, A68
- Brown, R. A. 2005, *ApJ*, 624, 1010
- Burrows, C. J., Krist, J. E., Stapelfeldt, K. R., and the WFPC2 Investigation Definition Team 1995, *BAAS*, 187.3205
- Burrows, A., Marley, M., Hubbard, W. B., et al. 1997, *ApJ*, 491, 856
- Butler, R. P., Marcy, G. W., Williams, E., McCarthy, C., Dosanji, P., & Vogt, S. S. 1996, *PASP*, 108, 500
- Cabrera, J., Fridlund, M., Ollivier, M., et al. 2009, *A&A*, 506, 501
- Campbell, B., Walker, G. A. H., & Yang, S. 1988, *ApJ*, 331, 902
- Chabrier, G., Baraffe, I., Allard, F., & Hauschildt, P. 2000, *ApJ*, 542, 464
- Charbonneau, D., Brown, T. M., Latham, D. W., & Mayor, M. 2000, *ApJ*, 529, L45
- Charbonneau, D., Berta, Z. K., Irwin, J., et al. 2009, *Nature*, 462, 891
- Chauvin, G., Lagrange, A.-M., Dumas, C., Zuckerman, B., Mouillet, D., Song, I., Beuzit, J.-L., & Lowrance, P. 2004, *A&A*, 425, L29
- . 2005, *A&A*, 438, L25
- Chauvin, G., et al. 2010, *A&A*, 509, A52+
- Chiang, E., Kite, E., Kalas, P., Graham, J. R., & Clampin, M. 2009, *ApJ*, 693, 734
- Chwolson, O. 1924, *Astronomische Nachrichten*, 221, 329
- Colón, K. D., Ford, E. B., Lee, B., Mahadevan, S., & Blake, C. H. 2010, *MNRAS*, 408, 1494
- Cochran, W. D., & Hatzes, A. P. 1993, in *Astronomical Society of the Pacific Conference Series*, Vol. 36, *Planets Around Pulsars*, ed. J. A. Phillips, S. E. Thorsett, & S. R. Kulkarni, (San Francisco, CA: ASP), 267–273
- Cumming, A. 2004, *MNRAS*, 354, 1165
- Deeg, H. J., Moutou, C., Erikson, A., et al. 2010, *Nature*, 464, 384
- Deming, D., Seager, S., Winn, J., et al. 2009, *PASP*, 121, 952
- Di Stefano, R., & Night, C. 2008, *arXiv:0801.1510*
- Dominik, M., Jørgensen, U. G., Rattenbury, N. J., et al. 2010, *Astronomische Nachrichten*,

- Doyle, L. R., Carter, J. A., Fabrycky, D. C., et al. 2011, *Science*, 333, 1602
- Eddington, A. S. 1920, *Cambridge Science Classics*, Cambridge: University Press, 134
- Einstein, A. 1936, *Science*, 84, 506
- Eisner, J. A., & Kulkarni, S. R. 2001, *ApJ*, 550, 871
- Erikson, A., Santerne, A., Renner, S., et al. 2012, *A&A*, 539, A14
- Erskine, D. J., & Ge, J. 2000, in *Astronomical Society of the Pacific Conference Series*, Vol. 195, *Imaging the Universe in Three Dimensions*, ed. W. van Breugel & J. Bland-Hawthorn, (San Francisco, CA: ASP), 501–+
- Fabrycky, D. C., Lissauer, J. J., Ragozzine, D., et al. 2012, arXiv:1202.6328
- Ford, E. B., Ragozzine, D., Rowe, J. F., et al. 2012, arXiv:1201.1892
- Fressin, F., Torres, G., Rowe, J. F., et al. 2012, *Nature*, 482, 195
- Gaudi, B. S., Albrow, M. D., An, J., et al. 2002, *ApJ*, 566, 463
- Gaudi, B. S., Bennett, D. P., Udalski, A., et al. 2008, *Science*, 319, 927
- Gaudi, B. S. 2010, in *Exoplanets*, ed. S. Seager (Tucson:University of Arizona Press), p79
- Gaudi, B. S. 2012, *ARA&A*, 50, 411
- Gilliland, R. L., Chaplin, W. J., Dunham, E. W., et al. 2011, *ApJS*, 197, 6
- Gorbikov, E., Brosch, N., & Afonso, C. 2010, *Ap&SS*, 326, 203
- Gould, A. 2000, *ApJ*, 535, 928
- Gould, A., & Gaucherel, C. 1997, *ApJ*, 477, 580
- Gould, A., Loeb, A. 1992, *ApJ*, 396, 104
- Gould, A., Ford, E. B., & Fischer, D. A. 2003a, *ApJ*, 591, L155
- Gould, A., Pepper, J., & DePoy, D. L. 2003b, *ApJ*, 594, 533
- Gould, A., Dorsher, S., Gaudi, B. S., & Udalski, A. 2006, *Acta Astron.*, 56, 1
- Gould, A., Dong, S., Gaudi, B. S., et al. 2010, *ApJ*, 720, 1073
- Gray, D. F. 1997, *Nature*, 385, 795
- Green, J., Schechter, P., Baltay, C., et al. 2011, arXiv:1108.1374
- Griest, K., & Safizadeh, N. 1998, *ApJ*, 500, 37
- Griffin, R. 1973, *MNRAS*, 162, 243
- Hatzes, A. P., & Cochran, W. D. 1993, *ApJ*, 413, 339
- Hatzes, A. P., Cochran, W. D., Endl, M., McArthur, B., Paulson, D. B., Walker, G. A. H., Campbell, B., & Yang, S. 2003, *ApJ*, 599, 1383
- Hatzes, A. P., Cochran, W. D., & Johns-Krull, C. M. 1997, *ApJ*, 478, 374
- Hatzes, A. P., Cochran, W. D., Endl, M., et al. 2006, *A&A*, 457, 335
- Hearnshaw, J. B., Abe, F., Bond, I. A., et al. 2006, *The 9th Asian-Pacific Regional IAU Meeting*, (Indonesia, Bali: Nusa Dua), 272
- Henry, G. W., Marcy, G. W., Butler, R. P., & Vogt, S. S. 2000, *ApJ*, 529, L41
- Hinkley, S., Oppenheimer, B. R., Zimmerman, N., et al. 2011, *PASP*, 123, 74
- Holman, M. J., & Murray, N. W. 2005, *Science*, 307, 1288
- Holtzman, J. A., Watson, A. M., Baum, W. A., et al. 1998, *AJ*, 115, 1946
- Horne, K., Snodgrass, C., & Tsapras, Y. 2009, *MNRAS*, 396, 2087
- Ida, S., & Lin, D. N. C. 2004, *ApJ*, 604, 388
- Johnson, J. A., Winn, J. N., Cabrera, N. E., & Carter, J. A. 2009, *ApJ*, 692, L100
- Kalas, P. & Jewitt, D. 1995, *AJ*, 110, 794
- Kalas, P., Graham, J. R., & Clampin, M. 2005, *Nature*, 435, 1067
- Kalas, P., et al. 2008, *Science*, 322, 1345

- Kane, S. R., Mahadevan, S., von Braun, K., Laughlin, G., & Ciardi, D. R. 2009, *PASP*, 121, 1386
- Kasdin, N. J., Vanderbei, R. J., Spergel, D. N., & Littman, M. G. 2003, *ApJ*, 582, 1147
- Kasting, J. F., Whitmire, D. P., & Reynolds, R. T. 1993, *Icarus*, 101, 108–128
- Kennedy, G. M., & Kenyon, S. J. 2008, *ApJ*, 673, 502
- Kiraga, M., & Paczynski, B. 1994, *ApJ*, 430, L101
- Lagrange, A.-M., Gratadour, D., Chauvin, G., et al. 2009, *A&A*, 493, L21
- Larson, A. M., Irwin, A. W., Yang, S. L. S., Goodenough, C., Walker, G. A. H., Walker, A. R., & Bohlender, D. A. 1993, *PASP*, 105, 825
- Latham, D. W., Stefanik, R. P., Mazeh, T., Mayor, M., & Burki, G. 1989, *Nature*, 339, 38
- Latham, D. W. 2012, *New A Rev.*, 56, 16
- Lazorenko, P. F., et al. 2011, *A&A*, 527, A25+
- Léger, A., Rouan, D., Schneider, J., et al. 2009, *A&A*, 506, 287
- Libbrecht, K. G. 1988, *ApJ*, 330, L51
- Liebes, S. 1964, *Physical Review*, 133, 835
- Lissauer, J. J. 1987, *Icarus*, 69, 249
- Lissauer, J. J., Fabrycky, D. C., Ford, E. B., et al. 2011, *Nature*, 470, 53
- Lissauer, J. J., Marcy, G. W., Rowe, J. F., et al. 2012, *arXiv:1201.5424*
- Lodge, O. J. 1919, *Nature*, 104, 354
- Lyne, A. G., & Bailes, M. 1992, *Nature*, 355, 213
- Macintosh, B. A., Graham, J. R., Palmer, D. W., et al. 2008, *Proc. SPIE*, 7015, 701518-701518-13
- Makarov, V. V., Beichman, C. A., Catanzarite, J. H., et al. 2009, *ApJ*, 707, L73
- Mao, S., Paczynski, B. 1991, *ApJ*, 374, L37
- Marcy, G. W., & Benitz, K. J. 1989, *ApJ*, 344, 441
- Marcy, G. W., & Butler, R. P. 1992, *PASP*, 104, 270
- Marcy, G. W., & Butler, R. P. 1995, in *Bulletin of the American Astronomical Society*, Vol. 27, *Bulletin of the American Astronomical Society*, (Washington, DC: AAS), 1379–+
- Marois, C., Lafrenière, D., Doyon, R., Macintosh, B., & Nadeau, D. 2006, *ApJ*, 641, 556
- Marois, C., Macintosh, B., Barman, T., Zuckerman, B., Song, I., Patience, J., Lafrenière, D., & Doyon, R. 2008, *Science*, 322, 1348
- Marois, C., Zuckerman, B., Konopacky, Q. M., Macintosh, B., & Barman, T. 2010, *Nature*, 468, 1080
- Mayor, M., & Queloz, D. 1995, *Nature*, 378, 355
- Mazeh, T., et al. 2000, *ApJ*, 532, L55
- McArthur, B. E., Benedict, G. F., Barnes, R., et al. 2010, *ApJ*, 715, 1203
- McBride, J., Graham, J.R., Macintosh, B., Beckwith, S.V.W.B., Marois, C., Poyneer, L.A., and Wiktorowicz, S.J. 2011, *PASP*, 123, 692
- McCullough, P. R., Stys, J. E., Valenti, J. A., et al. 2005, *PASP*, 117, 783
- Michel, E., & Baglin, A. 2012, *Proceedings of the Second CoRoT Symposium*, *arXiv:1202.1422*
- Mordasini, C., Alibert, Y., & Benz, W. 2009, *A&A*, 501, 1139
- Morton, T. D., & Johnson, J. A. 2011, *ApJ*, 738, 170
- Mouillet, D., Larwood, J.D., Papaloizou, J.C.B., and Lagrange, A.M. 1997, *MNRAS*, 292, 896
- Muirhead, P. S., Johnson, J. A., Apps, K., et al. 2012, *ApJ*, 747, 144

- Muterspaugh, M. W., et al. 2010, *AJ*, 140, 1657
- 1992, *Nature*, 355, 187
- Nutzman, P., & Charbonneau, D. 2008, *PASP*, 120, 317
- O’Toole, S. J., Tinney, C. G., Jones, H. R. A., et al. 2009, *MNRAS*, 392, 641
- Paczynski, B. 1986, *ApJ*, 304, 1
- Park, B.-G., Jeon, Y.-B., Lee, C.-U., & Han, C. 2006, *ApJ*, 643, 1233
- Pepe, F., Lovis, C., Ségransan, D., et al. 2011, *A&A*, 534, A58
- Pepper, J., Gould, A., & Depoy, D. L. 2003, *Acta Astron.*, 53, 213
- Pepper, J., & Gaudi, B. S. 2005, *ApJ*, 631, 581
- Pollack, J. B., Hubickyj, O., Bodenheimer, P., et al. 1996, *Icarus*, 124, 62
- Pollacco, D. L., Skillen, I., Collier Cameron, A., et al. 2006, *PASP*, 118, 1407
- Pravdo, S. H., & Shaklan, S. B. 2009, *ApJ*, 700, 623
- Queloz, D., Mayor, M., Sivan, J. P., Kohler, D., Perrier, C., Mariotti, J. M., & Beuzit, J. L. 1998, in *Astronomical Society of the Pacific Conference Series*, Vol. 134, *Brown Dwarfs and Extrasolar Planets*, ed. R. Rebolo, E. L. Martin, & M. R. Zapatero Osorio, 324–+
- Refsdal, S. 1964, *MNRAS*, 128, 295
- Rhie, S. H., Bennett, D. P., Becker, A. C., et al. 2000, *ApJ*, 533, 378
- Sako, T., Sekiguchi, T., Sasaki, M., et al. 2008, *Experimental Astronomy*, 22, 51
- Schneider, J., Dedieu, C., Le Sidaner, P., Savalle, R., & Zolotukhin, I. 2011, *A&A*, 532, A79
- Schuh, S. 2010, *Astronomische Nachrichten*, 331, 489
- Seager, S. 2010, *Exoplanet Atmospheres: Physical Processes* (Princeton: Princeton University Press)
- Southworth, J., Hinse, T. C., Jørgensen, U. G., et al. 2009, *MNRAS*, 396, 1023
- Shvartzvald, Y., & Maoz, D. 2012, *MNRAS*, 419, 3631
- Smith, B.A. & Terrile, R. J. 1984, *Science*, 226, 1421
- Snodgrass, C., Horne, K., & Tsapras, Y. 2004, *MNRAS*, 351, 967
- Steffen, J. H., & Agol, E. 2005, *MNRAS*, 364, L96
- Struve, O. 1952, *The Observatory*, 72, 199
- Torres, G., Andersen, J., & Giménez, A. 2010, *A&A Rev.*, 18, 67
- Tsapras, Y., Street, R., Horne, K., et al. 2009, *Astronomische Nachrichten*, 330, 4
- Udalski, A., Szymanski, M., Kaluzny, J., et al. 1993, *Acta Astron.*, 43, 289
- Udalski, A., Szymanski, M., Kaluzny, J., et al. 1994, *Acta Astron.*, 44, 227
- Udalski, A. 2003, *Acta Astron.*, 53, 291
- Udalski, A. 2009, *The Variable Universe: A Celebration of Bohdan Paczynski*, 403, 110
- Unwin, S. C., Shao, M., Tanner, A. M., et al. 2008, *PASP*, 120, 38
- van de Kamp, P. 1986, *Space Sci. Rev.*, 43, 211
- Veras, D., Ford, E. B., & Payne, M. J. 2011, *ApJ*, 727, 74
- Vogt, S. S. 1987, *PASP*, 99, 1214
- Walker, G. A. H., Yang, S., Campbell, B., & Irwin, A. W. 1989, *ApJ*, 343, L21
- Walker, G. A. H., Bohlender, D. A., Walker, A. R., et al. 1992, *ApJ*, 396, L91
- Winn, J. N. 2010, *Exoplanets*, 55
- Wolszczan, A., & Frail, D. A. 1992, *Nature*, 355, 145
- Wolszczan, A., Hoffman, I. M., Konacki, M., Anderson, S. B., & Xilouris, K. M. 2000, *ApJ*, 540, L41
- Wolszczan, A. 2012, *New A Rev.*, 56, 2
- Wright, J. T. 2005, *PASP*, 117, 657

Wright, J. T., & Howard, A. W. 2009, ApJS, 182, 205
Wright, J. T., et al. 2011, PASP, 123, 412
Wyatt, M.C., et al., 1999, ApJ, 527, 918
Yee, J. C., Shvartzvald, Y., Gal-Yam, A., et al. 2012, arXiv:1201.1002